Faculty of Physics and Astronomy
University of Heidelberg

Diploma thesis
in Physics

submitted by
Matthias Kohnen
born in Bocholt
2008

Ultracold Fermi Mixtures in an Optical Dipole Trap

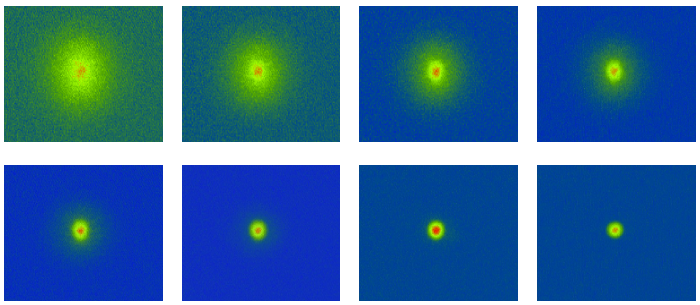

This diploma thesis has been carried out by

Matthias Kohnen at the

Max-Planck-Institute for Nuclear Physics

under the supervision of

Juniorprofessor Dr. Selim Jochim

This thesis reports on experiments with dilute gases consisting of distinguishable fermions whose interaction can be tuned over a wide range. These experiments cover the creation of a molecular Bose-Einstein Condensate (mBEC) as well as the first experiments on a three component degenerate Fermi mixture.

To create a mBEC we start with a magneto-optical trap (MOT) of 2×10^8 fermionic $^6\,\mathrm{Li}$ atoms. At a temperature of $410\,\mu\mathrm{K}$ a mixture of the two lowest hyperfine states of $^6\mathrm{Li}$ is transferred into an optical dipole trap and evaporatively cooled. These fermions are bound to bosonic molecules as soon as their temperature drops below their binding energy. Further cooling leads to condensation of these molecules into a mBEC of about 100000 particles at a temperature of approximately $30\,\mathrm{nK}$.

Further experiments make use of the wide tunability of the interaction between the three lowest hyperfine states of $^6\,\mathrm{Li}$ by means of Feshbach resonances. Employing RF transitions between these states allows for creating a mixture of three distinguishable fermions. This was achieved for the first time in our experiment. The produced sample contains 50000 atoms in each state at a temperature of $215\,\mathrm{nK}$, which corresponds to a $T/T_F = 0.37$. The process of creation and first experiments on such a sample are described here as well.

Diese Arbeit beschreibt Experimente an einem verdünnten Gas aus unterscheidbaren Fermionen, deren Wechselwirkung über einen weiten Bereich variiert werden kann. Diese Experimente reichen von der Erzeugung eines molekulare Bose-Einstein Kondensates (mBEC) bis hin zu den weltweit ersten Experimenten mit einer entarteten Mischung aus drei unterscheidbaren Fermionen.

Der Ausgangspunkt zur Erzeugung eine mBECs ist eine magneto-optische Falle (MOT) mit 2×10^8 fermionischen $^6\mathrm{Li}$ Atomen. Bei einer Temperatur von $410\,\mu\mathrm{K}$ wird eine Mischung aus den beiden tiefsten Hyperfeinzuständen in eine optische Dipolfalle geladen und dort evaporativ gekühlt. Aus den Fermionen bilden sich bosonische Moleküle, sobald ihre kinetische Energie unter ihre Bindungsenergie fällt. Weiteres Kühlen führt zur Kondensation dieser Moleküle in ein mBEC aus circa 100000 Teilchen mit einer Temperatur von ungefähr $30\,\mathrm{nK}$.

Weiter Experimente nutzen die weite Durchstimmbarkeit der Wechselwirkung zwischen den drei niedrigsten Hyperfeinzuständen des $^6\mathrm{Li}$. Unter Verwendung RF-induzierter Spinflips kann eine Mischung aus drei unterscheidbaren Fermionen erzeugt werden, was erstmal in unserem Experiment gelang. Unsere Mischung enthält 50000 Atome jeden Spinzustandes mit einer Temperatur von $215\,\mathrm{nK}$, was einem $T/T_F = 0,37$ entspricht. Der Erzeugungsprozeß und erste Experimente an solch einer Mischung werden ebenfalls beschrieben.

Contents

Chapter 1

Introduction

1.1 Overview

Ultracold quantum gases are an ideal model system for a vast variety of matter systems from almost all physical subjects. Though they are not realized in nature, their investigation contributed fundamentally to our understanding of matter. For quantum physics - from single particle to statistical - this seems obvious. Introducing optical lattices, the behavior of the particles is determined by the periodic structure of the lattice, comparable to the situation of electrons in a crystal. Here the quantum gases serve as a model for solid state physics. Latest research claims that fermionic mixtures can even be a model system for a quark-gluon plasma and help understanding baryon formation. This gives the link to nuclear physics.

One of the important properties of the gas making theoretical describtion so simple is that the interactions in such gases can be restricted to contact interactions. This can be done because the effective range of the interaction is much smaller than the average interparticle distance. The important experimental feature is that many properties can be tuned nearly arbitrarily. The strength of the interactions can be varied by so-called Feshbach resonances. The strength of the external potential can be varied by changing the beam power of the beam forming the trap. Additionally the shape of the external potential can be varied by modulating the deflection of this beam with acuosto-optic modulators. The quantum nature is revealed because the temperature in suche gases reaches nK range. Here the phase space densities increases to the order of one and the gas becomes highly degenerate. All this provides excellent preconditions for examining quantum physics.

The first optical trapping of neutral atoms in a magneto-optical trap (MOT) in 1986 [1] opened the door to the experimental realization of these model systems. Though the gas in a MOT is as dilute as the gases in our sourroundings, the temperature in the μK range allows for the access of phase space densities more than

10^7 times higher than in a thermal gas at room temperature. With those traps degeneracy cannot be reached, but they are the first step towards experiments with far larger phase space densities.

The first highly degenerate quantum gas was created with the achievment of Bose-Einstein condensation (BEC) in 1995 by E.A. Cornell, C.A. Wieman [2] and W. Ketterle [3], who were awarded the Nobel prize for their work in 2001. The extension of the wavefunction over a macroscopic number of particles allows for the investigation of statistical quantum physics and reveal insight from a new perspective to the quantum nature of matter.

A further great step in the process of gaining control over particle behavior was the application of Feshbach resonances known from nuclear physics in atom-optical experiments [4]. They allow researchers a nearly arbitrary control over the interaction between atoms by simply applying a magnetic field. Close to the resonance at high positive scattering length stable molecules can be formed [5]. These molecules can be condensated into a molecular BEC, which was first achieved by the groups of D. Jin [6], R. Grimm [7] and W. Ketterle [8] in 2003. On the other side of the resonance the scattering length is negative and the attractive meanfield interaction allows for the creation of weakly bound Cooper pairs in momentum space. The formation of such pairs of electrons in presence of small attractive interaction was successfully applied to explain superconductivity in metals by J. Bardeen, L. N. Cooper and J. R. Schrieffer in 1957 [9]. Hence it is called BCS regime. The crossover between the two sides is reversible and adiabatic and therefore isentropic. On top of the resonance the scattering length becomes infinite. The behavior of the particles at this point is no longer determined by the properties of the specific fermions or the scattering length, but simply by the momentum of the particles. This regime is called unitarity. Making use of this crossover a highly degenerate Fermi gas can be created. This can be done by first producing a BEC from molecules consisting of two fermions and afterwards increasing the magnetic field until the molecules are transformed into Cooper pairs [10] [11]. This provides a BCS regime with control over many relevant parameters, which hopefully will help to gain a better understanding of their physics, e.g. the physics of superconductors.

1.2 Experimental goals

Our experimental work aims at the creation of a finite degenerate Fermi gas. The idea is to create a molecular BEC on the side of the resonance where scattering lengths are positive and load it into a micro trap. Afterwards the magnetic field is ramped over the resonance, creating a highly degenerate Fermi gas. An aspheric lens and a EM-CCD camera will be used to perform high resolution imaging of

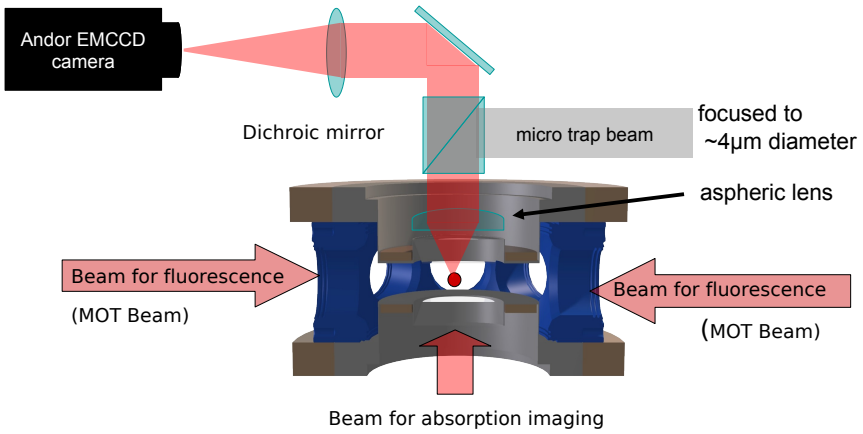

Figure 1.1: Setup for the micro trap and the high resolution imaging. Currently under construction.

the sample with single particle resolution.

The same asphere will be used to form the micro trap with a far red detuned laser beam focused to a diameter of a few μm (see figure 1.1). The large level spacing in such a tight trap will allow for very precise control over the number of atoms in the trap. If everything works well, we will be able to create, control and image a degenerate Fermi gas consisting of a few 10 particles. For the first time this will allow for testing many body theories, which describe the regime between single particle and statistical physics. The possibility to tune the shape of the potential via two crossed AOMs and the interaction between the particles by means of Feshbach resonances offers the possibility to examine a wide field of interesting physics in such an experimental system. It gives hope to gain better understanding about few fermion systems like electrons in the shell of atoms or nuclei in their cores. For example, it might be possible to examine shell formation and get a better understanding of this still not fully understood phenomenon.

Shortly after the production of our first molecular BEC we started experimenting with RF spectroscopy. RF fields enable the transfer of atoms between the three lowest hyperfine states of ^{6}Li. Inspired by enriching discussions with C. Greene we tried to create a three component Fermi mixture. This has never been done before experimentally, though all experimental techniques are standard today in an

atom optical laboratory. The theoretical discussion, however, has been very vivid over the past few years. Especially the stability of such a gas and the form of the ground state are discussed controversially. It is hoped that such a system has similarities with a quark gluon plasma, because the three color charges could behave analog to the three different spin states used in the experiment. Findings from such an experiment can possibly enhance the understanding of baryon formation or contribute to the explanation of the so-called color superconductivity [12]. Our first results support the assumption that intriguing physics can be observed in this system.

1.3 Content

This thesis starts with an overview over the standard techniques used to cool and trap neutral atoms. This part is followed by a comprehension of the physics of Feshbach resonances and the basic properties of bosonic and fermionic gases. The third chapter describes the setup of our experiment, focusing on the setup and the performance of the dipole trap. It is followed by two chapters reporting the key results of our experiments obtained during the last few months. The results are split up in a chapter dealing with the creation of a molecular BEC, which was achieved in February this year and a chapter dealing with the first results concerning a three component Fermi mixture. The thesis closes with a short conclusion and an outlook over the next steps planned in the experiment.

Chapter 2

Degenerate quantum gases

2.1 Trapping and cooling of neutral atoms

2.1.1 Scattering forces

On the way towards an ultracold gas, the main requirements are efficient cooling and trapping of atoms. In the last few decades, a remarkable toolbox for these purposes has been established. In experiments with neutral atoms the initial trapping and cooling from room temperature makes use of the radiation pressure of near-resonant laser beams. A laser beam with a slight detuning against the atomic transition exhibits a force on an atom moving against the propagation direction of the beam. To calculate this force, we use a simplified semi-classical picture: The atom can only be in two states, a ground state and an excited state. The light field is treatend as a classical electro-magnetic field:

The atoms in the ground state absorb photons from the beam. Assuming a low power laser field with respect to the saturation intensity, the photons are emitted spontaneously, which means that there is no preferred direction for the emission. Summing up over many of these processes only the incoming photons transmit a momentum of $\hbar k$ to the atom in the direction of the beam. To calculate the scattering force the scattering rate of photons has to be determined. This rate depends on the intensity of the light $s_0 = \frac{I}{I_s}$ in terms of the saturation intensity I_s and the detuning of the laser towards the atomic transition $\delta = \omega_0 - \omega_L$ and is found to be

$$\gamma_P = \frac{s_0 \Gamma/2}{1 + s_0 + \left[2\left(\delta + \omega_D\right)/\Gamma\right]^2} \tag{2.1}$$

where Γ is the natural line width of the atoms. When moving relative to the laser source, the atoms see the laser frequency with a Doppler shift of $\omega_D = \vec{k}\vec{v}$. Neglecting stimulated emission, the force induced by all scattered photons results

$\vec{F}_C = \hbar\vec{k}\gamma_P$. This force is fundamental for all atom manipulation with a near resonant laser field.

Making use of these forces a dissipative potential can be created, in which atoms are trapped and cooled down to the order of a few hundred μK. For further cooling the heating induced by the resonant photons has to be avoided and the dissipative potential has to be replaced by a conservative one. For this purpose either magnetic traps or optical dipole traps are used. The magnetic traps employ the magnetic moment of the atoms to trap them in a magnetic field. The optical dipole traps induce a dipole moment on the atoms and then trap them in an extremum of the electro-magnetic field. However, these traps only trap the atoms in position. Cooling is obtained via evaporation of the hottest atoms and subsequent thermalization. Since we are employing all of these methods (except for magnetic trapping, which is only used for alignment purposes), a short explanation of these tools will be given in the following. Most of these subjects are described in detail in the last two diploma theses of our group ([13],[14]), so this section is kept rather short and only summarizes the main features.

2.1.2 Slowing with radiation pressure

The experiment is supplied with $^6\mathrm{Li}$ atoms from an oven at a temperature of $350°C$ to provide a sufficient vapor pressure and therefore adequate particle flux. Their velocities follow a thermal Maxwell-Boltzmann distribution with its peak value at $\widehat{v} = \sqrt{2k_BT/m_{\mathrm{Li}}} \approx 1300\,\mathrm{m/s}$ where k_B is Boltzmann's constant and m_{Li} the mass of a $^6\mathrm{Li}$ atom. Since the magneto-optical trap (MOT) can only capture particles with a velocity up to $50\,\mathrm{m/s}$ the atoms have to be precooled in a so-called Zeeman slower. A Zeeman slower is a laser beam counter-propagating the direction of the atomic beam. A varying magnetic field around the beam ensures that the atoms stay in resonance with the laser beam. When they slow down, the changing Doppler detuning is compensated by the changing magnetic field due to the Zeeman effect. In our setup this enhances the maximal initial particle velocity for capturing to a value of $800\,\mathrm{m/s}$, which is about $13.7\,\%$ of the total particle flux.

2.1.3 Trapping in position space

The magnetic field at the end of the Zeeman slower is produced by the coils of the MOT. A MOT employs a magnetic quadrupole field and the Zeeman effect to obtain a position dependence of the radiation forces and create a dissipative potential for the atoms. The resonant photons come from two counter-propagating beams in all three directions of space. The light force depends strongly on the detuning of the laser towards the atomic transition. The used laser beams are not

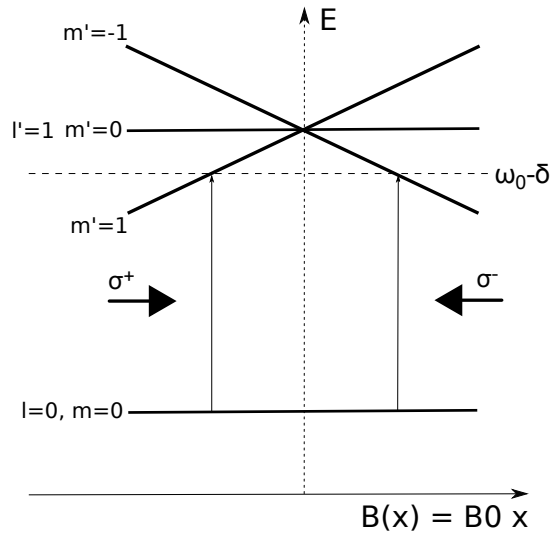

Figure 2.1: Energy scaling with magnetic field of the different sublevels and laser configuration for a MOT

in resonance with the atoms at zero field. Hence in the center of the trap no force is exhibited on the atoms. When the atoms try to leave the trap, their energy levels are shifted and come into resonance with the laser the moment they reach a sufficient magnetic field. Therefore they are slowed down and pushed back towards the center of the trap. It is important that the polarization of the counterpropagating light matches the transition that comes into resonance with the beam. When the polarization is fixed for one transition, transitions to other states are forbidden because of angular momentum conservation. Only for a configuration as given in figure 2.1 the correct transitions for cooling can be driven.

The limit of this cooling mechanism is given by the heating of the randomly emitted photons. To derive a quantity for the lowest reachable temperature, the quadratic statistical dispersion has to be regarded, for the mean momentum itself vanishes. Taking the time derivative of this quantity results the heating rate

$$(\Delta p^2)_N = \overline{p^2} - \overline{p}^2 = N\hbar^2k^2 - 0 \quad \Rightarrow \quad \frac{d}{dt}(\Delta p^2)_N = \hbar^2k^2\frac{dN}{dt} = D\,.$$

For dN/dt the photon scattering rate γ_P given in equation 2.1 can be inserted. The constant D is therefore fully determined.

The force the laser beams exert on the atoms is simply the sum over the two counter-propagating laser beams considering the different sign of their velocities

with respect to the movement of the atom. For low temperatures, that is small kinetic energies, the expression can be expanded in a power series in v. Combining all prefactors from the scattering force to α, this yields the following differential equation for p^2:

$$F = -\alpha m v \quad \Rightarrow \quad \frac{d}{dt}p = -\alpha p \quad \Rightarrow \quad \frac{d}{dt}p^2 = 2p\frac{d}{dt}p = -2\alpha p^2 \,.$$

Now the two forces can be compared. A connection with the temperature can be introduced by using the equivalence of thermal energy $E_{th} = 3/2 k_B T$ and kinetic energy $E_{kin} = p^2/(2m)$:

$$p^2 = 3mk_BT = \frac{1}{2\alpha}\frac{d}{dt}(p^2) = \frac{D}{2\alpha} \,.$$

Inserting the definitions of D and α yields a term for the lowest reachable temperature:

$$k_BT = -\frac{\hbar\Gamma}{2}\frac{1+(2\delta/\Gamma)^2}{4\delta/\Gamma} \,. \tag{2.2}$$

This term reaches a minimum at $\delta = -\Gamma/2$, which is called the Doppler limit. Inserting the natural line width of ^{6}Li results a Doppler limit of $\approx 140\,\mu$K for our MOT. Cooling below the Doppler limit can be obtained using polarization gradient or Raman cooling. For our setup this would mostly lead to a factor of $1/10$ in temperature and the effort in the setup is large compared to the gain in temperature. That is why it is not used in the experiment. For further explanations on cooling with resonant light, the reader may be referred to [15] or one of the other standard textbooks dealing with this subject.

2.1.4 Dipole traps

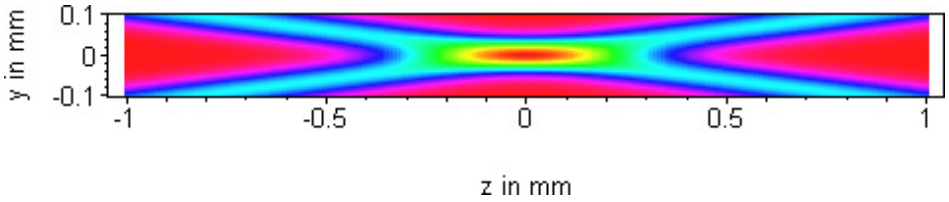

Figure 2.2: Potential of a crossed dipole trap with the properties given in the text. The sketch shows a cut trough the y-z plane at $x = 0$.

To cool far below the Doppler limit the atoms have to be trapped without resonantly scattering photons. To do so, the atomic cloud is loaded from the MOT into

a dipole trap consisting of a far red detuned laser beam with a Gaussian shape. The dipole potential for a neutral atom with complex polarizability α in a laser beam with intensity I is given as

$$U_{dip} = -\frac{1}{2}\left\langle \vec{p}\vec{E} \right\rangle = -\frac{1}{2\epsilon_0 c}\Re(\alpha)\, I(\vec{r}) \tag{2.3}$$

(cp. [16]). The atom in the laser field can be described with a classical harmonic oscillator model. In this a model the oscillator has the eigenfrequency of the atomic transition ω_0, is driven by the external field with frequency ω and damped by classic dipole radiation with the rate Γ_ω. Solving the equation of motion results the complex polarizability of the atom:

$$\alpha = 6\pi\epsilon_0 c^3 \frac{\Gamma/\omega_0^2}{\omega_0^2 - \omega^2 - i\,(\omega^3/\omega_0^2)\,\Gamma} \tag{2.4}$$

with the on-resonance damping rate $\Gamma = (\omega_0/\omega)^2\,\Gamma_\omega$. Combining equation 2.3 and equation 2.4 yields the dipole potential:

$$U_{dip}\,(\vec{r}) = -\frac{3\pi c^2}{2\omega_0^3}\left(\frac{\Gamma}{\omega_0 - \omega} + \frac{\Gamma}{\omega_0 + \omega}\right) I\,(\vec{r})\ . \tag{2.5}$$

For the scattering rate equation 2.4 leads to

$$\Gamma_{sc} = \frac{P_{abs}}{\hbar\omega} = \frac{1}{\hbar\epsilon_0 c}\Im(\alpha)\, I(\vec{r}) =$$

$$\frac{3\pi c^2}{2\hbar\omega_0^3}\left(\frac{\omega}{\omega_0}\right)^3\left(\frac{\Gamma}{\omega_0 - \omega} + \frac{\Gamma}{\omega_0 + \omega}\right)^2 I\,(\vec{r}) \tag{2.6}$$

where we used that the total power absorbed can be calculated as $P_{abs} =< \dot{\vec{p}}\vec{E} >= \frac{\omega}{\epsilon_0 c}\Im(\alpha)\, I(\vec{r})$.

Taking into account the actual situation in the setup a few numbers relevant for the experiment can be derived: The potential formed by two crossed Gaussian beams can be calculated from the intensity distribution of a Gaussian beam as given in [17]

$$I(r,z) = \frac{2P}{\pi W^2(z)}\exp\left(-\left[\frac{2r^2}{W^2(z)}\right]\right). \tag{2.7}$$

Here $W(z)$ denotes the waist of the beam at position z which can be calculated to be

$$W(z) = W_0\left[1 + \left(\frac{z\lambda}{\pi W_0^2}\right)^2\right]^{1/2}. \tag{2.8}$$

W_0 denotes the minimal waist of the beam and λ the wavelength of the trapping laser beam. In our experiment these values are given as $W_0 = 50\,\mu\mathrm{m}$ and $\lambda = 1070\,\mathrm{nm}$. The total potential can then be estimated by summing over two beams rotated by $+\alpha/2$ and $-\alpha/2$. α is the crossing angle of the two beams, which in our case is measured to be $14°$. Assuming z as the propagation direction of the beam we can write $r^2 = x^2 + y^2$ and rotate the beams in the y-z plane. Combined with equation 2.5 the potential can directly be calculated, when inserting Γ_{Li} and the angular frequencies of the atomic transition $\omega_0 = 2\pi c/\lambda_{\mathrm{Li}}$ and of the dipole laser $\omega = 2\pi c/1070\,\mathrm{nm}$. For a laser power of $P = 200\,\mathrm{W}$ this leads to a peak potential depth in terms of temperature of $\widehat{U}_{dip}/k_B = 4.2\,mK$. That means that the efficiency of the transfer process from the MOT to the dipole trap is only limited by the density of the gas in the MOT and the spatial overlap of both traps and not by the depth of the dipole trap.

The potential of a Gaussian beam can be approximated harmonically in its center. In most experimental situations the potential depth is an order of magnitude larger than the average thermal energy of the particles, so approximating the trap harmonically is valid in most cases. Since theoretical treatment becomes much more simple when assuming a harmonic trap, this approximation is widely used. In this case, the trap can be characterized by giving the eigenfrequencies of the harmonic oscillator in the symmetry directions. To calculate these trap frequencies the term for the trapping potential can be expanded into a power series. With the coefficient for the second order term U_2 and the expression for the energy carried by a particle in a harmonic oscillator $E_{ho} = 1/2m\omega^2 r^2$ the trap frequencies in the particular direction can be written as $f = \sqrt{2U_2/m_{Li}}/(2\pi)$. Here m_{Li} is the mass of a ^{6}Li atom. As an example, the trap frequencies at a beam power of $35\,\mathrm{mW}$ are given: The trap depth at this beam power is $\widehat{U}_{dip}/k_B = 1\,\mu\mathrm{K}$ and the sample in our trap is an almost pure BEC. The trap frequencies are $f_{axial} = 30\,\mathrm{Hz}$ for the z direction and $f_{rad} = 243\,\mathrm{Hz}$ in the y direction. The aspect ratio turns out to be $f_{rad}/f_{axial} = 8.16$. Figure 2.2 gives a plot of the potential in the z-y plane at $x = 0$.

2.1.5 Evaporative cooling

In a dipole trap the atoms are only caught in position space. Cooling is obtained by evaporation of the hottest atoms. The particles having a thermal energy larger than the trap depth leave the trap. Via scattering with other atoms the sample rethermalizes at a lower temperature. In momentum space this can be imagined as cutting off the tail of the Boltzmann distribution and restoring it with the remaining particles under consideration of energy conservation.

The critical value for condensation is the phase space density. In a harmonic

trap it is given as $\rho = N(\hbar\overline{\omega}/k_B T)^3$, with $\overline{\omega} = (\omega_x\omega_y\omega_z)^{1/3}$ being the mean trap frequency. In a thermal cloud at room temperature the phase space density is in the order of 10^{-11} and has to reach unity for condensation. The experimentalist decreases $\overline{\omega}$ with the beam power. Hence efficient evaporation is achieved by trapping a large number of particles at low temperatures. This section shall give a theoretical description of the evaporation process and provide a basis for the evaluation of its efficiency.

In a trap with a given depth U and a mean temperature T there are $\exp(-U/k_B T)$ atoms able to leave the trap. The exponent $U/k_B T \equiv \eta$ is called truncation parameter and roughly describes the progress of evaporation at a certain trap depth. At a fixed trap depth, a larger η corresponds to a colder sample, but at the same time this means that further evaporation will take more time. In experiments the evaporation is usually compensated by heating processes when η reaches the order of 10.

Following [18] we assume that a particle leaving the trap takes its potential energy U and a certain part $\alpha k_B T$ of the thermal energy with it. Here α denotes a parameter depending on η and varying between 0 and 1. The exact form depends on the shape of the trap and turns out to be $\alpha = (\eta - 5)/(\eta - 4)$ for a harmonic potential if $kT \ll U$. The average potential energy is half the total energy $\overline{E} = E/2$, hence lowering the potential depth leads to an additional energy loss of the system. Summing up over all terms yields

$$\dot{E} = \dot{N}\left(U + \alpha k T\right) + \frac{\dot{U}}{U}\frac{E}{2}\,. \tag{2.9}$$

Taking into account that the time derivative of the thermal kinetic energy is given by $\dot{E} = 3Nk_B\dot{T} + 3\dot{N}k_B T$, it is possible to calculate a connection between the change of the potential depth and the particle number:

$$\frac{N(t)}{N_0} = \left(\frac{U(t)}{U_0}\right)^{\frac{3}{2(\eta+\alpha-3)}}\,. \tag{2.10}$$

As mentioned, the phase space density of the cloud is the critical value for condensation. Considering that the mean oscillator frequency $\overline{f} \propto \sqrt{U}$ and $T \propto U$ the scaling of the phase space density with the trap depth and the atom number can be calulated:

$$\frac{\rho(t)}{\rho_0} = \left(\frac{U(t)}{U_0}\right)^{-\frac{3(\eta+\alpha-4)}{2(\eta+\alpha-3)}} = \left(\frac{N(t)}{N_0}\right)^{-(\eta+\alpha-4)}\,. \tag{2.11}$$

The only parameter that can be influenced in the experiment is η. For a small η heating and loss processes in the trap, e.g. of the laser, have to be reduced. But since high values of η are accompanied by slow evaporation a compromise

between efficient and fast evaporation within the boundary conditions given by the trap has to be found. The estimations made above will allow to quantitatively evaluate the quality of the trap and the evaporation process.

2.2 Feshbach resonances of ^{6}Li

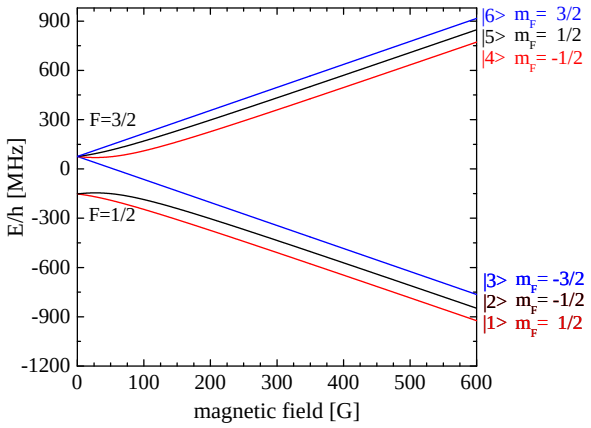

Figure 2.3: Hyperfine splitting of the two lowest energy states of ^{6}Li in dependence of the magnetic field.

2.2.1 Scattering

Scattering between two particles in quantum physics can be described by the so-called partial wave expansion. The scattered wave function is expanded into partial waves according to their angular momentum. With increasing energy involved in the scattering process, higher order partial waves participate. The whole scattering process can then be described by the accumulation of phase shifts δ_l in the partial waves, which reduces the contribution of the l-th partial wave to the total cross section σ_{tot} to

$$\sigma_l = \frac{4\pi}{k^2}\,(2l+1)\sin^2\delta_l \tag{2.12}$$

for non-identical particles. Since $\delta_l \propto k^{2l+1}$, for low temperatures ($k \to 0$) only the energetically lowest s-waves contribute to the scattering process. This makes scattering very simple to describe, because the wave function is simply a superposition of an incoming plane wave and a scattered spherical wave. The scattered wave is isotropic and contains no angular momentum. The cross section is given

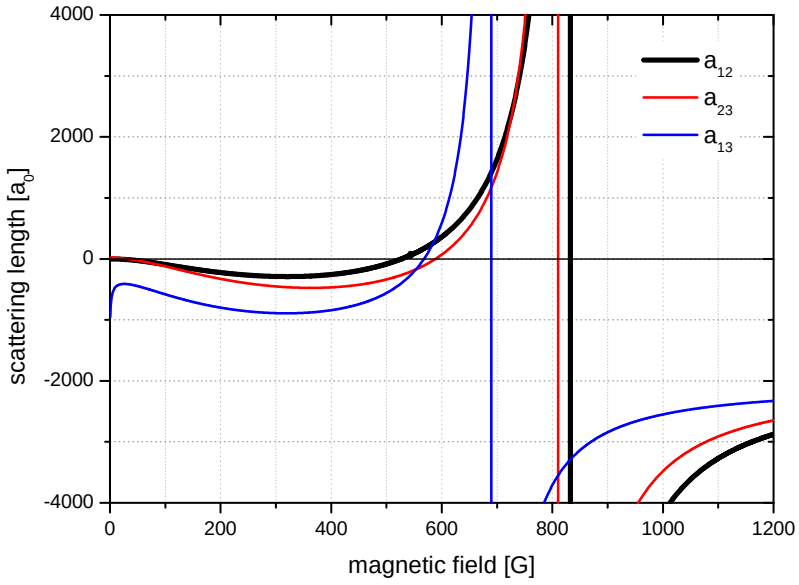

Figure 2.4: Feshbach resonances of the three lowest hyperfine states of ^{6}Li. The plot shows the scattering length a in units of Bohr's radius in dependence of the magnetic field [19].

as $\sigma_{tot} = \sigma_0 = 4\pi a^2$. The only parameter still influencing the scattering in this regime is the so-called s-wave scattering length a.

The scattering cross section can be imagined as an effective extension of the particle for the actual interaction. For low energies, this extension is given by the scattering length. The cross section is therefore proportional to a^2. However, the cross section cannot exceed the expansion of the wave packet given by the de-Broglie wave length $\lambda_{dB} = 2\pi/k$. Thus when the scattering length diverges, the cross section is no longer determined by the scattering length but by the momentum of the particles $\sigma \propto 1/k^2$. To calculate the cross section in regimes between these extrema a simple interpolation turns out to describe reality quite well (cp. [20]):

$$\sigma = \frac{4\pi a^2}{1 + k^2 a^2} \,. \tag{2.13}$$

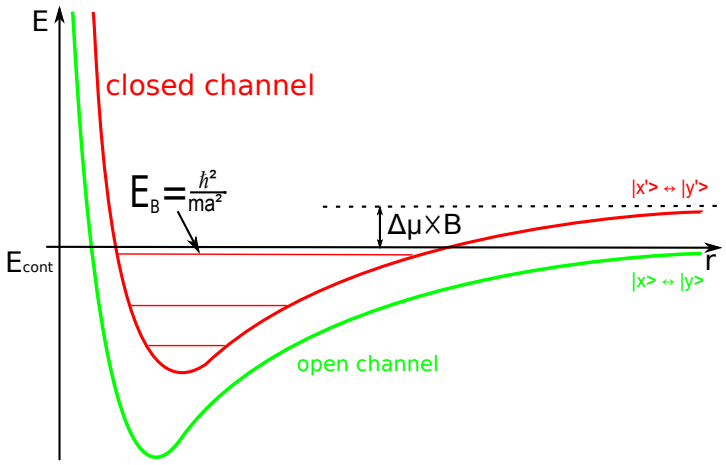

Figure 2.5: A Feshbach resonance occurs when a bound state of a closed channel lies in the vicinity of the continuum of an open channel. The relative position of the two channels can be tuned with a magnetic field. If the bound state lies slightly below the continuum, molecules with a binding energy of $E_B = \hbar^2/ma^2$ can be formed.

2.2.2 Hyperfine states of ^{6}Li

Since two identical fermions cannot interact with each other via s-wave interactions due to symmetry reasons, at least two non-identical particles have to be involved to achieve scattering in a fermionic sample at low temperatures. This is necessary to perform evaporation and to reach ultracold temperatures. As a second particle species other bosonic isotopes of the fermion or completely other particles can be choosen. These particles sympathetically cool the fermions. The third and experimentally most simple option is to use different spin states of the same fermions, as it is done in our experiment. Figure 2.3 shows the Zeeman energies of the lowest hyperfine states of ^{6}Li and their scaling with the magnetic field. Since we load our dipole trap with fermions in the state $F = 1/2$, we naturally work with a mixture of the two different spin states $m_F = 1/2$ and $m_F = -1/2$. The third state that scales negative with increasing magnetic field and that is of relevance for this thesis is the $|F = 3/2, m_F = -3/2\rangle$. For convenience, the states are numbered ascending from the lowest. This nomenclature will be used throughout this thesis. In an RF field, transitions between the $|1\rangle \leftrightarrow |2\rangle$ and the $|2\rangle \leftrightarrow |3\rangle$ states can be driven. The transition between $|1\rangle$ and $|3\rangle$ is forbidden in first order due to angular momentum conservation.

A reason for choosing ^{6}Li for our experiment is that the scattering length of all three of the lowest hyperfine states can be tuned over a wide range with a magnetic offset field. The field to access the full range of scattering length is

quite comfortably to reach. On the other hand, the width of the tuning regime is wide enough so that the necessary stability of the magnetic field is accessable without too much effort. Figure 2.4 gives an overview of the scattering length versus magnetic field for all three combinations of these states. The bold one is the $|1\rangle \leftrightarrow |2\rangle$ resonance, which is the important resonance for our first BEC. The others become relevant in the last part of this thesis, where the creation of a stable mixture of three distinguishable fermions is presented.

2.2.3 Tuning interactions

One of the great features of the experiment is the nearly arbitrary tunability of the scattering length between two particles via a scattering resonance. By means of a magnetic offset field the scattering length is tuneable from a zero crossing to infinite positive values on the one side of the resonance and from infinite negative to the background scattering length on the other side. At large positive scattering lengths this allows to experiment with bound fermions forming bosons in a repulsive meanfield and create a BEC. On the other side, negative scattering lengths lead to weakly bound fermions in an attractive mean-field forming a BCS-like system. The crossover is continuous in all parameters, meaning that the systems undergoes no phase transition but a smooth transfer from one side of the resonance to the other. The repulsive interaction of the molecules on the BEC side is smoothly taken over by the Fermi repulsion of the free fermions on the BCS side. At the position where the scattering length becomes infinite, the behavior of the particles becomes independent of all other parameters and is only determined by the momentum of the fermions. It is equal for all fermion combinations and is therefore called unitary. The isentropy of the crossover allows to create a highly degenerated Fermi gas, when producing a BEC at the side of the resonances where the scattering lengths is positive and afterwards ramp up the magnetic field so that the scattering length changes its sign and molecules transform into weakly bound Cooper pairs. Such resonances were first predicted in nuclear physics by Herman Feshbach [21] and are therefore called Feshbach resonances. The underlying process of such resonances is described in the following:

The scattering potential between two particles in a well defined state is called a channel. Changing the internal state of one of the particles leads to a different channel with a different interaction potential and a different magnetic moment. The channels therefore tune slightly different with the magnetic field. A channel is called closed, if its continuum lies above the energy of the incoming particles, which means that they cannot access the channel without violating energy conservation. It is called open, if the continuum of the channel degenerates with the kinetic energy of the incoming particles or lies lower.

A Feshbach resonance occurs, when a bound state of a closed channel lies close

to the continuum of the open channel (cp. figure 2.5). If the channels are coupled to each other, e.g. via hyperfine interaction, the particles can virtually enter the bound state, but due to energy conservation they have to leave it again after a time proportional to the inverse of the energy difference between the continuum and the bound state. This results in a coupling process between the particles of second order. If the bound state lies closely beneath the continuum, a third particle can carry away energy and momentum difference and molecules with a binding energy $E = \hbar^2/ma^2$ can be formed. Note that this equation is only valid as long as the scattering length is large compared to the range of the van-der-Waals interaction. This is the case in our experiment, because the range of the van-der-Waals interaction is typically below $100a_0$ and the scattering lengths in our experiment lie in the range of a few thousand a_0. Here a_0 denotes Bohr's radius.

If the scattering channels have different magnetic momenta, the relative position of the bound state and the continuum can be tuned by simply changing the magnetic field: $\Delta E = \Delta\mu B$. The scattering length then tunes with the magnetic field as:

$$a(B) = a_{bg}\left(1 - \frac{\Delta}{B - B_0}\right) \tag{2.14}$$

where a_{bg} is the background scattering length, B_0 is the position and Δ the width of the resonance. Note that the width of the resonance depends quadratically on the coupling strength, which reflects that the scattering is a second order process. For the $|1\rangle \leftrightarrow |2\rangle$ these values were found to be $a_{bg} = -1405a_0$, $B_0 = 834.149\,\mathrm{G}$ and $\Delta = 300\,\mathrm{G}$ [22].

2.3 Bose-Einstein condensation

The main observables in the experiment are distributions of particles in position and in momentum space, because these are the values that can be obtained directly with the imaging system. The shape of a trap formed by two beams crossed under a small angel has the form of a cigar. The harmonic approximation of the center of such a trap yields nearly two equal frequencies $\omega_x = \omega_y = \omega$ in the directions perpendicular to the symmetry axis of the beam propagation and a larger one $\lambda\omega_z = \omega$ in line with this axis. λ is the inverse of the aspect ratio of the trap and in our current setup $\lambda \approx 1/10$. Since this is the relevant situation in our experiment, the following calculations will be done assuming such a trap.

The bosonic sample undergoes a phase transition during condensation. That is why there is a region in which we have a sample containing condensed and uncondensed parts. Observing a bimodal distribution which reveals the existence of a thermal and a condensed part is still the smoking gun to prove that condensation

has actually been reached. Therefore, the critical temperature and the condensate fraction in dependence of temperature are further values which are of interest for the experimentalist. The discussion is done following [23].

2.3.1 Spatial and momentum distribution

The spatial ground state distribution of a Bose-Einstein condensate (BEC) can be calculated very easily in the Thomas-Fermi approximation, which is derived in the following.

Since Bose-Einstein condensation is a many-body phenomenon, it is an adequate approach to start with the many body Hamilton operator for N interacting bosons in an external potential V_{ext}:

$$\mathbf{H} = \int d\vec{r}\mathbf{\Psi}^\dagger(\vec{r}) \left[-\frac{\hbar^2}{2m}\nabla^2 + V_{ext}(\vec{r}) \right] \mathbf{\Psi}(\vec{r}) +$$

$$\frac{1}{2}\int d\vec{r}d\vec{r'}\mathbf{\Psi}^\dagger(\vec{r})\mathbf{\Psi}^\dagger(\vec{r'})V(\vec{r}-\vec{r'})\mathbf{\Psi}(\vec{r})\mathbf{\Psi}(\vec{r'}) \tag{2.15}$$

where $\mathbf{\Psi}^\dagger(\vec{r})$ and $\mathbf{\Psi}(\vec{r})$ are the creation and annihilation field operators for a boson at position $\vec{r}$ and $V(\vec{r}-\vec{r'})$ is the interaction potential between two particles. Inserting this Hamiltonian into the Heisenberg equation the time evolution of the field operator can be written as:

$$i\hbar\frac{\partial}{\partial t}\mathbf{\Psi}(\vec{r},t) = [\mathbf{\Psi}, \mathbf{H}] =$$

$$\left[-\frac{\hbar^2}{2m}\nabla^2 + V_{ext}(\vec{r}) + \int d\vec{r'}\mathbf{\Psi}^\dagger(\vec{r'},t)V(\vec{r'}-\vec{r})\mathbf{\Psi}(\vec{r'}) \right] \mathbf{\Psi}(\vec{r},t)\,. \tag{2.16}$$

Up to this point, the equation is exact and in general solvable with numerical methods. However, the calculations become quite lengthy and complicated for large N. They become much simpler, if the field operator $\mathbf{\Psi}(\vec{r},t)$ is replaced by a classical field $\Phi(\vec{r},t)$. The first idea is to replace the field operator by its expectation value $\Phi(\vec{r},t) = \langle\mathbf{\Psi}(\vec{r},t)\rangle$. The absolute square of this function is the density distribution of the ground state, that is the condensate. Since the phase of the field is also well defined, this parameter can be used to describe the order in the system. The field changes dramatically when the system undergos a phase transition to the condensate phase and has therefore the meaning of an order parameter. The function looks like the ground state function for a single particle, and although it is not a single particle probability density function but a many particle density distribution it is called the wave function of the condensate. The kinetic term and the term for the external potential only change slightly by this

replacement. But for the integral over the interaction potential this simplification yields in general no good results, since the contribution of many particles to the interaction has to be taken into account. However, if the sample is dilute and the interatomic distance is large compared to the effective range of the interactions, the interaction can be restricted to two body scattering in an effective delta potential $V(\vec{r'} - \vec{r}) = g\delta(\vec{r'} - \vec{r})$. Furthermore, it can be assumed that the energy involved is very small, so the strength of the interaction g depends only on the s-wave scattering length a and g can be calculated as $g = 4\pi\hbar^2 a/m$. This yields an equation for the ground state wave function Φ

$$i\hbar\frac{\partial}{\partial t}\Phi(\vec{r},t) = \left(-\frac{\hbar^2}{2m}\nabla^2 + V_{ext}(\vec{r}) + g\left|\Phi(\vec{r},t)\right|^2\right)\Phi(\vec{r},t) \tag{2.17}$$

called the Gross-Pitaevskii equation (GPE) [24]. Because the Hamiltonian is time-independent, the time evolution can be seperated by writting

$$\Phi(\vec{r},t) = \Phi(r)\exp\left(-i\mu t/\hbar\right). \tag{2.18}$$

This allows to execute the time derivative on the left side and makes the time dependence drop out:

$$\mu\Phi(\vec{r}) = \left(-\frac{\hbar^2}{2m}\nabla^2 + V_{ext}(\vec{r}) + g\left|\Phi(\vec{r})\right|^2\right).\Phi(\vec{r}). \tag{2.19}$$

This equation is called the time-independent GPE. If the interaction energy of the particles is large compared to their kinetic energy, the kinetic term can be neglected. This conditions can qualitatively be written as $Na/a_{ho} \gg 1$. Here $a_{ho} = \sqrt{(\hbar/m_{\mathrm{Li}}\omega\lambda^{1/3})}$ is the harmonic oscillator length, the relevant length scale to characterize the trapping potential. The parameter Na/a_{ho} is called the Thomas-Fermi parameter and will occure in the equations for most of the relevant properties of the condensate. The GPE can now be written as:

$$\mu\Phi(\vec{r}) = \left(V_{ext}(\vec{r}) + g\left|\Phi(\vec{r})\right|^2\right)\Phi(\vec{r}). \tag{2.20}$$

This equation called the Thomas-Fermi equation. Since the particle number distribution is proportional to the absolute square of the wave function, this quantity can easily be derived:

$$n(\vec{r}) = \left|\Phi(\vec{r},t)\right|^2 = \frac{\mu - V_{ext}(\vec{r})}{g}. \tag{2.21}$$

This formula results of course only physical values, if $\mu > V_{ext}(\vec{r})$ since the absolute square of a wave function cannot be negative. Outside a certain radius R_k the wave function $\Phi(\vec{r})$ drops to zero. R_k can be obtained by solving $\mu = V_{ext}(R_k)$ with respect to R_k.

Knowing the coupling between the particles g and the external potential given as a harmonic oscillator potential $V_{ext}(\vec{r}) = \sum_{k=1}^{3} \frac{1}{2} m\omega_k^2 r_k^2$, leaves just a short calculation for the chemical potential. It is given by the boundary condition that the integral of the density distribution over the whole space has to yield the total particle number $N = \int n(\vec{r}) d^3r$:

$$\mu = \frac{\hbar\omega}{2} \left(\frac{15Na}{a_{ho}} \right)^{2/5} . \tag{2.22}$$

Now we can also compute the extension R_k of the condensate in the direction x_k by solving $\mu = \frac{1}{2}\omega_k^2 R_k^2$ which yields:

$$R_k = \lambda^{\frac{1}{3}} a_{ho} \left(\frac{15Na}{a_{ho}} \right)^{1/5} \frac{\omega}{\omega_k} \tag{2.23}$$

The momentum distribution can then simply be obtained by Fourier transforming the resulting density distribution:

$$n(\vec{p}) = N \frac{15}{16\hbar^3} R^3 \left(\frac{J_2(\widetilde{p})}{\widetilde{p}^2} \right)^2 . \tag{2.24}$$

Here $R = (R_x R_y R_z)^{1/3}$ is the mean condensate expansion and $\hbar^2\widetilde{p}^2 = (p_x^2 R_x^2 + p_y^2 R_y^2 + p_z^2 R_z^2)$ is the scaled total momentum. $J_2(x)$ denotes the second order Bessel function. Note, however, that the interaction energy for the values of a reached in our experiments is much larger than the kinetic energy. So the expansion in a time of flight measurement will mainly be determined by the interaction of the particles.

2.3.2 Critical temperature and condensate fraction

Estimating the condensate fraction is simply estimating the number of particles in the ground state. Estimating the critical temperature T_C for condensation to set in is calculating the point, where this number becomes macroscopic. Neglecting interaction between the particles the distribution in energy space is given by the Bose-Einstein distribution:

$$n(\epsilon_i) = \frac{1}{\exp\left(\beta(\epsilon_i - \mu)\right) - 1} \tag{2.25}$$

with $\beta = (k_B T)^{-1}$. Assuming again a harmonic oscillator potential, the eigenenergies ϵ_i of the system are known. Condensation sets in, when all particles are in excited states and adding a particle would take the energy it takes to add a particle to the ground state. The energy necessary to add one particle to a system is given by the chemical potential. Hence the second condition is fulfilled by

setting $\mu = \epsilon_0$. Assuming a small level spacing compared to the total energy of the system, the sum over the excited states can be replaced by an integral. The integral does not weight the zero point. Therefore, the particles in the ground state are not counted, but the integral results only the particles in the excited state. This leaves us with the following equation to solve for $\beta(T_C)$:

$$N = \int dn_x dn_y dn_z \frac{1}{\exp\left[\beta\hbar(\omega_x n_x + \omega_y n_y + \omega_z n_z)\right] - 1} \,. \tag{2.26}$$

The result turns out to be

$$k_B T_C = \hbar\omega \left(\frac{\lambda N}{\zeta(3)}\right)^{1/3} \tag{2.27}$$

with $\zeta(x)$ is the Riemann function and $\zeta(3) \approx 1.202$. The condensate fraction in dependence of temperature results immediately when taking into account that $N_0 + N_T = N$:

$$\frac{N_0}{N} = 1 - \left(\frac{T}{T_C}\right)^3 \,. \tag{2.28}$$

Note that these equations only hold in the case of non-interacting bosons. Taking interaction into account complicates the whole calculations a lot. But since the scattering length in our experiments reaches a few thousand Bohr radii this equations have to be used very carefully. A first order correction term for the critical temperature has been found by Giorgini *et al.* [25]:

$$\frac{\delta T_C}{T_C^0} = -1.32 a \sqrt{\frac{m\omega}{\hbar}} \left(\lambda N\right)^{1/6} \,. \tag{2.29}$$

T_C^0 is the transition temperature calculated for the non-interacting case. However, since this formula leads to corrections in the order of $20\,\%$ in the actual situation in our experiment, even higher order corrections have to be taken into account to find values that agree with our measurements.

2.3.3 Bimodal distribution

Below the critical temperature the atomic cloud will start to condense. Imaging the cloud will lead to a bimodal distribution, revealing a Gaussian shaped part for the thermal cloud, and a inverted parabola for the condensate part. Having a closer look reveals that the thermal part itself is not a simple Gaussian. At low temperatures the bosonic nature of the particles has to be taken into account and the Boltzmann distribution has to be replaced by the Bose-Einstein distribution.

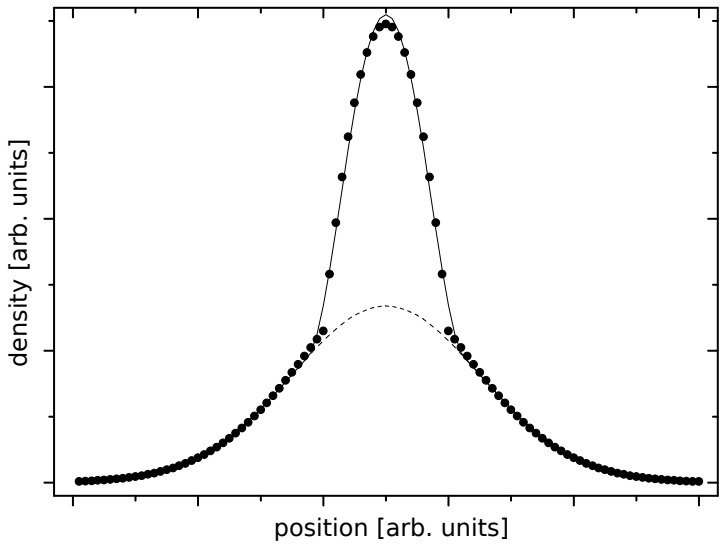

Figure 2.6: Fit of a simple BEC model to a distribution where the interaction between thermal and condensate part had been taken into account. The points are calculated with the model presented in section 2.3.3, the fit is a simple bimodal fit with a inverted parabola added to a Gaussian. As one can observe the deviations are very small and can therefore be neglected in the evaluation.

When solving the integrals occurring in these calculations, the polylogarithmic functions appear. They are defined as $g_p(z) = \sum_{k=1}^{\infty} z^k/k^p$.

The density distribution can be calculated by integrating the Bose-Einstein distribution for particles in a harmonic trap over momentum space. The effective potential that has to be inserted into the equation is given as the sum over the external potential V_{ext} and the meanfield interaction energy $2gn(\vec{r})$:

$$n_T(\vec{r}) = \int d^3p \frac{1}{\exp\beta\left[p^2/2m + V_{ext}(\vec{r}) + 2gn(\vec{r})\right] - 1} \tag{2.30}$$

$$\Rightarrow n_T(\vec{r}) = \frac{1}{\lambda_{th}^3} g_{3/2}\left(e^{-\beta(V_{ext}(\vec{r})+2gn(\vec{r}))}\right) \tag{2.31}$$

with $\lambda_{th}^2 = 2\pi\hbar^2/mk_BT$ is called the thermal deBroglie wavelength. In general $n(\vec{r}) = n_T(\vec{r}) + n_0(\vec{r})$ with n_T being the thermal and n_0 being the condensate particle distribution function. Solving this problem is difficult, since the coupled differential equation cannot be solved analytically. But regarding that the thermal

cloud is very dilute, its density compared to the density in the condensate can be neglected:

$$n_T(\vec{r}) = \frac{1}{\lambda_{th}^3} g_{3/2}\left(e^{-\beta(V_{ext}(\vec{r})+2gn_0(\vec{r}))}\right) . \tag{2.32}$$

The distribution for the condensate itself is given by equation 2.21, reduced by the interaction of the thermal cloud. But as mentioned above, the effects of the weak meanfield interaction in the dilute thermal gas can be neglected. For the fit the function has to be restricted to the region where it is valid by multiplying equation 2.21 with the step function $\Theta(x)$. This avoids the distribution from producing negative output:

$$n_0(\vec{r}) = \frac{\mu - V_{ext}(\vec{r})}{g}\Theta(\mu - V_{ext}(\vec{r})) . \tag{2.33}$$

However, since the atomic cloud is too dense for our imaging system, we can only observe the momentum distribution after a certain time-of-flight. The small deviations in the starting conditions for the thermal part will certainly blur out during the time-of-flight and a normal Gaussian momentum distribution will be observed. In the condensate part, the effects of the dilute thermal cloud can even be neglected in the distribution in position space. Since the kinetic energy of the atoms is small compared to the meanfield energy, it will be possible to calculate the distribution after the time-of-flight by simply assuming a transformation of the meanfield energy into kinetic energy. This will be sufficient to get a good description by the fit.

Yet, since the scattering length of $^6\,\mathrm{Li}$ and therefore the meanfield energy of the condensate is very large, the width of the condensate after a time-of-flight is hard to distinguish from the thermal part. According to equation 2.22 $\mu = \mu(a)$ and we can influence the interaction in and therefore the expansion of the condensate part. We will make use of this feature later to obtain the bimodal distribution by ramping down the magnetic field and so the scattering length a. This results a clear difference between both parts after a time-of-flight of about $10\,\mathrm{ms}$.

2.4 Degenerate Fermi gases

In this part, density and momentum distribution for a cold fermionic sample in a harmonic trap are calculated according to [26]. The key parameters of the gas are the chemical potential and the Fermi energy, that is the energy up to which the energy levels are filled at zero temperature. These will be the first quantities that have to be calculated. To simplify the calculations they are done assuming a non-interacting Fermi gas. This is of course not the case in the experiment, but

the considerations can help to understand the physics of the system and lead to a rough estimation of the relevant values.

2.4.1 Fermi energy and chemical potential

We assume again a cigar-shaped potential as described above with a potential $V(\vec{r}) = \frac{M\omega^2}{2}\left(x^2 + y^2 + \lambda^2 z^2\right)$ where ω is the radial and $\omega_a = \lambda\omega$ the axial trap frequency. The eigenvalues of this potential are:

$$\epsilon_{n_x,n_y,n_z} = \hbar\omega\left(n_x + n_y + \lambda n_z\right) . \tag{2.34}$$

Counting the number of states in a unity energy volume results the continuous density of states:

$$g(\epsilon_{n_x,n_y,n_z}) = \frac{\epsilon^2}{2\lambda\left(\hbar\omega\right)^3} . \tag{2.35}$$

The replacement is valid if the thermal energy is much larger than the average level spacing, which is the case in most experimental situations. For example, a trap with a frequency of $500\,\mathrm{Hz}$ has a depth in terms of temperature of $\approx 100\,\mathrm{nK}$ and a level spacing of about $0.6\,\mathrm{nK}$. Using the Fermi distribution and integrating over all particles yields an implicit expression for the chemical potential:

$$N = \int \frac{g(\epsilon)d\epsilon}{e^{\beta(\epsilon-\mu)} + 1} . \tag{2.36}$$

This equation can in general not be solved analytically for μ. To derive explicit results anyway, it is possible to restrict the consideration to the low and zero temperature case. Here equation 2.36 simplifies and becomes solvable.

In the case of zero temperature the Fermi-Dirac occupation factor

$$f(\epsilon) = \frac{1}{\exp\left(\beta(\epsilon - \mu)\right) + 1} \tag{2.37}$$

is one for energies smaller than the Fermi energy E_f and zero for energies larger, which makes the integral quite easy to solve. Only the integration of $g(\epsilon)$ from zero to E_f has to be obtained. Solving for N yields an expression for the Fermi energy:

$$E_f = \hbar\omega\left(6N\lambda\right)^{(1/3)} . \tag{2.38}$$

Note that the critical temperature in the BEC case scales in the same way with particle number and trap frequency, simply the prefactor is different for the two cases.

To get an expression for the chemical potential at low temperatures the Sommerfeld expansion can be used. The expansion makes use of the fact, that the derivative of the Fermi distribution for low temperature is only different from zero in a small area around the Fermi edge. Since at zero temperature the lowest energy levels simply fill up with particles under consideration of Pauli's exclusion law, the distribution in momentum space has a sharp edge at the momentum corresponding to the highest filled energy level. The step from unity to zero in the occupation number of the energy states is called the Fermi edge, which is widened when increasing temperature, because the particles in the highest state can access higher energy levels due to their thermal energy.

The Sommerfeld expansion gives a general solution for integrals of the form

$$I(T) = \int_{-\infty}^{\infty} dE g(E) f(E) \tag{2.39}$$

where $f(E)$ is the Fermi distribution, for low temperatures. The first step is now to execute a partial integration. If $g(E)$ drops to zero for $E \rightarrow -\infty$ and $g(E)$ will not diverge as fast as $\exp(E)$ with increasing E, the boundary values vanish. Since the derivative of $f(E)$ at low temperatures is only different from zero close to the Fermi edge, the remaining integrand can be expanded around $E = \mu$. Taking into account that only the even powers of $(E - \mu)$ contribute to the sum due to symmetry reasons, the integral can be expressed as (see [27]):

$$I(T) = \int_{-\infty}^{\mu} dE g(E) + 2 \sum_{n=1}^{\infty} (1 - 2^{1-2n}) \zeta(2n) \left(k_B T\right)^{2n} \left[\frac{d^{2n-1} g(E)}{dE^{2n-1}}\right]_{E=\mu} . \tag{2.40}$$

The equation looks quite complicated, but simplifies equation 2.36 such, that it can be solved for μ analytically, since at low energies only the first term of the sum has to be taken into account:

$$\mu(T, N) = E_F \left[1 - \frac{\pi^2}{3} \left(\frac{k_B T}{E_F}\right)^2\right] \tag{2.41}$$

2.4.2 Spatial and momentum distribution

It is possible to find analytical expressions for the density in momentum and position space for $T = 0$. A good starting point for this is to derive implicit equations for a continuous, semi classical picture and then evaluate the results for $T = 0$. These results give a good approximation to the values in the ultracold regime where our experiments take place and T is not greater than a few hundred nK.

Under the assumption that the particles can be described as wave packets located at a position $\vec{r}$ and with wave vector $\vec{k}$ the phase space distribution can be written by employing the Fermi distribution and replacing the energy with the Hamiltonian $H = H((\vec{r}), \hbar\vec{k})$. Normalizing to the density of states in the phase space $(2\pi)^{-3}$ yields the number density:

$$\omega(\vec{r}, \vec{k}; T, \mu) = \frac{1}{(2\pi)^3} \frac{1}{e^{\beta(H(\vec{r},\hbar\vec{k})} + 1} \,. \tag{2.42}$$

As a boundary condition the integral of the number density over the whole phase space has to result the total particle number N. This yields an implicit equation for the chemical potential. The distribution of states for the Hamiltonian is known. The momentum and spatial distribution can be derived after solving for the chemical potential. This is done by integrating over the other three dimension of the phase space and with this projecting the phase space distribution to the position or momentum space:

$$n(\vec{r}; T) = \int d^3\vec{k}\, \omega(\vec{r}, \vec{k}; T, \mu) \tag{2.43}$$

$$n(\vec{k}; T) = \int d^3\vec{r}\, \omega(\vec{r}, \vec{k}; T, \mu) \,. \tag{2.44}$$

For $T = 0$ things become quite simple again. The occupied space in $\vec{k}$ space is simply a sphere with the radius of the Fermi wave vector $\vec{k}_F$. Dividing through the density of states in phase space yields the density in position space. Since the Fermi energy is constant for the whole sample, but the trap potential $V(\vec{r})$ varies with position, a "local" Fermi energy can be defined in a way that potential and kinetic energy of the particles always sum up to the Fermi energy:

$$\frac{\hbar^2 k_F(\vec{r})^2}{2m} + V(\vec{r}) = E_F \,. \tag{2.45}$$

This helps to write the density distribution in position space for $T = 0$ as:

$$n(\vec{r}) = \frac{8N\lambda}{\pi^2 R_F^3} \left(1 - \frac{\rho^2}{R_F^2}\right)^{3/2} . \tag{2.46}$$

where $R_F^2 = 2E_F/m\omega_r^2$ is called the Fermi radius and $\rho^2 = x^2 + y^2 + \lambda^2 z^2$ is the effective distance from the center of the trap. Of course this equation only makes sense for $\rho < R_F$. The distribution drops to zero for all other values.

Note that the Fermi radius scales with ω^{-1}, whereas the expansion of a BEC scales with $\omega^{-2/5}$. Hence for low trap frequencies a bosonic cloud has a smaller extension than the fermionic one. This is a direct effect of the Fermi pressure induced by Pauli blocking.

To obtain the momentum distribution, the integral over the position space has to be executed. Since this distribution in the case of $T = 0$ is a step function, the integral becomes just the volume in position space occupied by states whose local Fermi wave vector is smaller than the absolute value of the wave vector for which the density is calculated. The positive and negative solutions of equation 2.45 for $\vec{r}$ result the upper and lower borders for the volume integral. This yields the density distribution in momentum space:

$$n(\vec{k}) = \frac{8N}{\pi^2 K_F^3} \left(1 - \frac{\left|\vec{k}\right|^2}{K_F^2} \right)^{3/2} , \tag{2.47}$$

where $K_F^2 = k_F(0)^2 = 2ME_F/\hbar^2$ is the global Fermi wave number. Note that the momentum distribution is isotropic even for the elliptic trap, whereas the spatial distribution is influenced by the shape of the trap.

2.4.3 Phase transition

In the bosonic case it was shown that there is a phase transition when the phase space density of the atomic cloud exceeds unity. In a non-interacting Fermi gas such a transition cannot be observed when increasing the phase space density. The gas becomes more and more degenerate until at zero temperature all energy levels are filled up to the Fermi energy. However, as Bardeen, Cooper and Schrieffer found out for the case of electrons in metals, an arbitrary weak interaction is sufficient to bind the fermions in momentum space to delocalized Cooper pairs. The pairs are no stable molecules, but a meanfield phenomenon. The particles have no fixed partner but form many-body pairs, meaning that two fermions are only associated with each other for a short time and then change their partner. In order to excite such a gas from the ground state at least one of the pairs has to be broken. This minimal excitation energy is called excitation gap and has been calculated to be

$$\Delta = \frac{1}{2} \left(\frac{2}{e} \right)^{7/3} E_F \exp\left(-\frac{\pi}{2k_F|a|} \right) \tag{2.48}$$

if the gas is homogeneous and the coupling is only mediated via s-wave scattering. The presence of such a gap is in nearly every case connected with superfluidity. So if a minimal interaction is present, the Fermi gas undergoes a phase transition into a superfluid state at a temperature proportional to the gap. It therefore depends

exponentially on the scattering length a and the Fermi wave number k_F

$$T_{BCS} = \frac{e^{\gamma}}{\pi}\left(\frac{2}{e}\right)^{7/3} T_F \exp\left(-\frac{\pi}{2k_F|a|}\right) \approx 0.277 T_F \exp\left(-\frac{\pi}{2k_F|a|}\right) \quad (2.49)$$

where $\gamma \approx 0.577216$ is Euler's constant. In a weak interacting gas the transition temperature is orders of magnitude smaller than the Fermi temperature. For example, taking the trap frequencies of the lowest trap we used so far with a typical particle number at background scattering length yields a transition temperature of $T_{BCS} = 10^{-4}\, T_C$. This regime cannot be reached with today's experiments. But with the help of Feshbach resonances the scattering length can be increased dramatically. Although the approximation above is only valid for small interactions, the transition energy for a Fermi gas at unitarity has been calculated to be $T_{BCS} = 0.2 T_C$. In this regime such a phase transition has been observed. The commonly accepted signature of the superfluid phase are so-called vortices, quantizised twirls in a rotating gas. Such vortices could be observed by the group of W. Ketterle [28] in 2005. The regime also seems to be reachable in our experiment, but the observation of vortices is still a difficult thing to do.

Chapter 3

Experimental setup and techniques

3.1 Vacuum and MOT

As in the preceding chapter this chapter will not go into details concerning the experimental setup that have already been described in-depth by the predecessors in the group. Up to the dipole trap, only the main facts will be summarized and the reader is referred to [13] for MOT performance and vacuum setup and [14] for details on the offset locks of MOT and imaging lasers.

Since every collision with a particle from the background gas leads to losses from the trap, the atomic cloud would immediately be destroyed at atmospheric pressure. This is why experiments have to be conducted in an ultra high vacuum. Therefore, the heart of the experiment is a vacuum chamber at a pressure of about $10^{-11} - 10^{-12}\,\mathrm{mbar}$. An overview over the vacuum setup with pumps and ^{6}Li-oven is given in figure 3.1.

The oven is heated to a temperature of $350\,^{\circ}\mathrm{C}$ to create a sufficient vapor pressure to supply the experiment with a suitable flux of $^6\,\mathrm{Li}$ atoms. After leaving the oven, the atoms enter the Zeeman slower, which decelerates them to about $50\,\mathrm{m/s}$. At this speed they can be trapped in the MOT. The MOT consists of three retro reflected beams and a quadrupole field, which makes it possible to trap the atoms in position space and precool them to about $410\,\mu\mathrm{K}$, so that they can be loaded into an optical dipole trap. The lasers of the MOT have to match the atomic transition very precisely and therefore, it is necessary to control the stability of the lasers with sub-MHz precision. This is done via Doppler-free saturation spectroscopy and offset locks. The offset locks enable to tune the frequency of the lasers with respect to the atomic transition. The whole setup for the creation of the MOT and imaging lasers is placed on a separate optical table and the beams are transferred to the actual experiment by optical fibres. This decouples these laser system from the dipole setup and saves valuable space around the octagon.

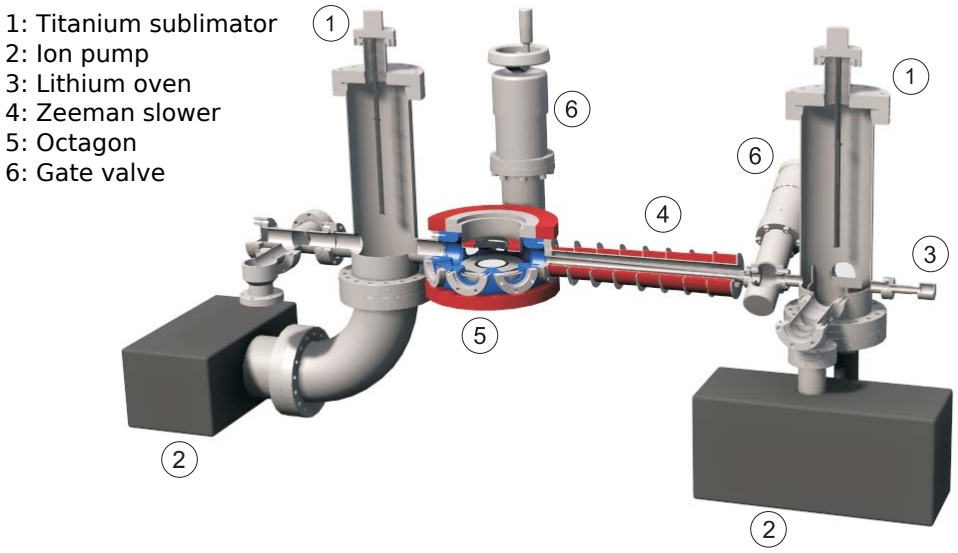

Figure 3.1: Overview over the vacuum setup with oven, pumps and experimental chamber. The red parts are the coils providing the magnetic field for the MOT and the Zeeman slower. The gate valve opens the oppurtunity to add parts to the experimental chamber without breaking the vacuum.

3.2 Imaging

A powerful tool to gather information about the atomic ensemble is to measure density distributions by imaging the particles in the cloud with resonant light. Note that at sufficient magnetic field the energy difference between the hyperfine states allows for independently imaging each component by tuning the frequency of the imaging beam. The imaging can be done via measuring the fluorescence of light that is scattered by the atoms or the other way around via measuring the absorption of photons from a resonant beam. It is not possible to observe the alignment of the beams in the chamber directly, so parameters like the spatial overlap of the MOT and the dipole beams can only be observed by the behavior of the atoms in the traps. Therefore the imaging of the atoms plays an important role even in aligning and optimizing the trap.

Fluorescence imaging is done by counting the photons scattered onto the camera. Considering that the scattering is isotrope, the number of atoms can be deduced from the scattering rate and the exposure time of the camera. As only a small fraction of the scattered photons is observed, many photons have to be scattered for a sufficient signal. For example, assuming a lens collecting the light within a diameter of $1'' \mathrel{\widehat{=}} 2.54\,\mathrm{cm}$ in a distance of $15\,\mathrm{cm}$ from the atomic cloud results a solid angle of 1.8×10^{-3} in which photons are collected. In the dipole trap the scattering rate of photons is much too small to get a image with a good signal-to-noise ratio. To get a sufficient number of photons, the cloud is recaptured into the MOT before performing such a measurement. Unfortunately, this also destroys all spatial information and the atom number is the only useable value that can be obtained from these measurements.

A more effective tool is the measurement of the absorption of photons from a resonant laser beam. The measurement counts all the photons that are not scattered in the direction of the camera. Since the dynamics of the sample are slow compared to the duration in which the laser beam is applied to the sample, nearly all spatial information of the atoms is preserved. Since the main observation tool in the presented experiments is absorption imaging, the calculations necessary to get the spatial density distribution from the images taken by the camera will briefly be pointed out.

In fact, for a single absorption image three pictures have to be taken: The absorption image itself, a reference picture with no atoms present and a background image, which is taken without turning on the imaging beam. By the imaging the 3D density distribution, it is integrated in the direction of the camera. The 2D optical density distribution can be calculated from the three pictures as

$$\rho_{op}(x,y) = -\ln \frac{I_{abs}(x,y) - I_{bg}(x,y)}{I_{ref}(x,y) - I_{bg}(x,y)}\,. \tag{3.1}$$

The optical density and the particle density are connected by the scattering cross section of the light with the atoms:

$$\sigma_{sc} = \frac{\rho_{op}}{n} = \frac{3\lambda^2}{2\pi}\,. \tag{3.2}$$

This formula for the cross section is valid for light matching the atomic transition, which in the given case would be circularly polarized light. However, since the imaging beam runs perpendicularly to the quantization axis given by the magnetic field, it cannot be polarized circularly. With the actually used horizontally polarized light we get only half the cross section. To evalute the image it is once again integrated, this time by the camera programm to increase the signal-to-noise ratio and to simplify evalutaion. The resulting 1D density distribution is fitted with a Gaussian. Since in most cases the particles follow a thermal momentum distribu-

tion, the Gaussian shape corresponds quite well with the measured density profile. Dividing the area under the curve by the scattering cross section σ_{sc} leads to the total number of particles

$$N = \frac{A_{gauss}}{\sigma_{sc}} \frac{A_{pixel}}{M^2} \tag{3.3}$$

where $A_{pixel} = 8.4\,\mu\mathrm{m} \times 19.6\mu\mathrm{m}$ is the total area of one pixel and $M = 1.17$ the magnification of our imaging system.

By measuring a density distribution, the distribution of the atomic cloud in momentum space can also be determined, when measuring the cloud after a certain time-of-flight (TOF). This kind of measurement is accomplished by instantly switching off all trapping potentials and leaving the atoms to a free flight for typically a few ms before imaging them. If the gas is thermal, the momentum is distributed according to the Maxwell-Boltzmann distribution, hence a Gaussian can be fitted to the expanded cloud. Assuming a very small initial expansion of the cloud compared to the width σ after the TOF, a simple calculation results the temperature of the cloud:

$$T = \frac{mv^2}{2k_B} = \frac{m_{Li}\sigma^2}{2(\Delta t)^2 k_B} \tag{3.4}$$

where Δt is the time between trap release and imaging.

However, for few fermion systems the limit for this kind of imaging is reached. If single particles should be resolved, the resolution of the imaging system has to be on the same order of magnitude as the object that shall be imaged. The resonant light "sees" the atoms with their cross section of about $(\lambda/2)^2$. With the asphere recently implemented into the setup our imaging system has a resolution of about $2\,\mu\mathrm{m} \approx 3\lambda$. This means that without enhancing the resolution by another factor of $3 - 4$ we will not be able to resolve single particles. When doing fluorescence imaging the resolution only has to be on the same order of magnitude as the interatomic distance, because the atoms are the sources of the photons. Hence, for this purpose it might be better to fall back on fluorescence imaging again. With the asphere we can collect photons in a solid angle of 10^{-1}. The precision with which the number N of incoming photons can be determined is limited by $\sqrt{N}$ due to the Poisson distribution of the counts. This effect is called shot noise. At least 10 photons have to be collected from each atom to get a signal that can clearly be distinguished from this noise. The photons will be detected with an EM-CCD camera (Andor iXon DC887BI), which will allow to reach the shot noise limit. Summing up, this results in a total number of 100 photons that has to be scattered from each atom for the measurement. The near future will show if it is possible to scatter the necessary number of photons without destroying spatial information before measuring it.

3.3 Dipole trap

3.3.1 Setup

The dipole trap is formed by a single mode Ytterbium doped fiber laser (IPG YLR-200-SM) with a center wavelength of $1070\,\mathrm{nm}$ and a line width of about $3\,\mathrm{nm}$. The laser can produce a maximum output power of $200\,\mathrm{W}$. The beam is focused to a diameter (twice the waist of a Gauss fit to the beam profile) of about $1.3\,\mathrm{mm}$ to fit through two acousto-optic modulators (AOMs)(Crystal Technology 3110-191 and -197). In an AOM the beam undergoes Bragg diffraction on a sound wave in a crytall. The sound wave in the crystall is produced by a piezoelectric crystall, driven with RF power. The AOMs are used on the one hand to control the laser power via varying the RF power and with that the diffraction efficiency of the AOM. On the other hand, this provides the possibility of creating time averaged potentials if the frequency of the RF signal and with that the diffraction angle of the AOMs are tuned much faster than the trap frequencies. The RF signal is produced by a VCO (Z-Communications V110-ME01) that can be tuned with a frequency of up to $10\,\mathrm{MHz}$, which is fast compared to the highest trap frequency of $18.4\,\mathrm{kHz}$ we can reach with the current setup. The power of the RF signal can be adjusted using a variable attenuator (Minicircuits ZX73-2500M-S+) before amplifying the signal to the desired power for optimal operation of the AOMs (amplifier: Minicircuits ZHL-03-5WF).

All diffraction orders except for the first one of both AOMs are filtered out in a water cooled beam dump. The remaining beam is enlarged to a diameter of about $4.1\,\mathrm{mm}$. In between the polarization of the beam can be tuned by a half wave plate to pass through a Brewster polarizer. The polarizer suppresses the polarization noise of the fiber laser with a specified extinction rate of 10^{-3}. This is done because the lifetime of the atoms in the trap highly depends on the relative polarization of the two counter propagating beams. We observed, that it is very critical for a long lifetime of particles in the trap, that the two beams are polarized orthogonally and that a slight misalignment leads to a significant decreament of the lifetime. That is why it is necessary to clean the polarization as good as possible.

The collimated beam is focused into the chamber using a lens with a focal length of $300\,\mathrm{mm}$ leading to a focus of $100\,\mu\mathrm{m}$ diameter. On the other side of the chamber the beam is recollimated, the polarization is rotated by 90° and the beam is refocused into the chamber, crossing the incoming beam in the center of the chamber at an angle of about 14°. Finally the beam is dumped into another water cooled beam dump.

Since the mirrors only reflect about 99.9% of the light, the transmitted beam can be used for monitoring purposes. In our setup this is done once behind the second mirror (counted in beam direction from the fiber coupler of the dipole laser) to

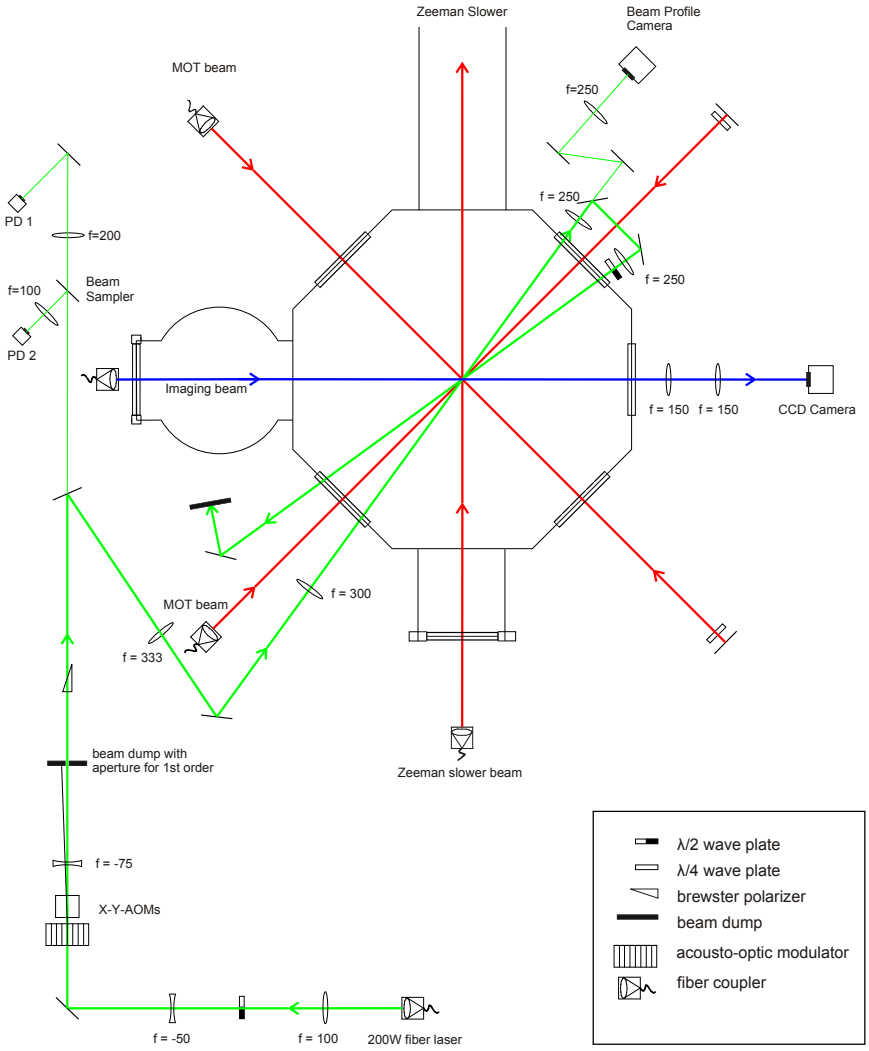

Figure 3.2: Optical setup around the vacuum chamber

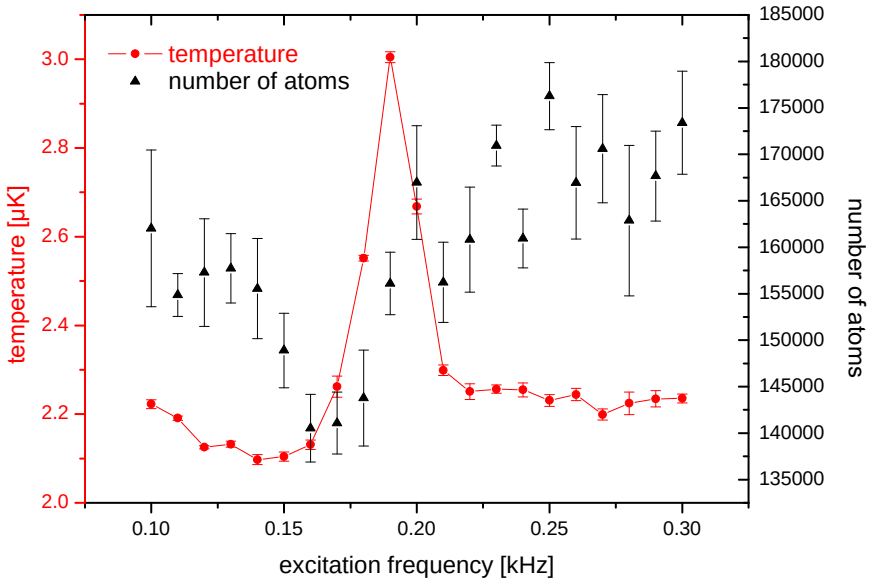

Figure 3.3: Measurement of the axial trap frequency at a laser power of $760\,\mathrm{mW}$. When shaking the trap with different frequencies, the temperature reaches a maximum at the double trap frequency. The errors are the statistical errors of at least five independent measurements.

monitor the power via two photo diodes and once behind the fourth to observe the beam profile with a CCD camera. The two photodiodes are necessary to measure the power over a wide range and a great sensitivity at low beam power. The wide range is covered with a silicon diode (Thorlabs PDA36A) with a large excitation gap compared to the energy of the infrared photons. Therefore, relatively high beam power can be measured without saturating the diode. The precision at low power is reached with a GaAs diode (Hamamatsu G8370-81). Because GaAs has a smaller excitation gap it is more sensitive to the infrared photons, which helps to improve signal-to-noise ratio at low beam intensities.

The shape of the beam in the focus can be observed with a focusing lens and a beam profile camera (DataRay, WinCamD). It is important to check the profile regularly since dust or other particles on the optics can lead to strong distortion of the beam due to thermal lensing effects, especially at high beam power.

Since we work with quite high laser power, thermal effects were an important issue when setting up the dipole trap. They occur when optical elements change their refractive structure due to the heat absorbed when the beam propagates through them. However, calculating those effects is not straight forward, since

a lot of simplifications have to be made to derive quantitive values. In our case it turned out that the experiment is the most reliable possibility to quantify these effects and to decide, whether the experiment will work with them or not. Here a short summary of the results of the analysis is given:

The optical isolator first implemented into the setup (LINOS Photonics FI-1060-8SI) contains a Terbium Gallium Garnet (TGG) crystal of $40\,\mathrm{mm}$ length. A beam collimated to a diameter of $4.3\,\mathrm{mm}$ at $10W$ was focused to a beam with a minimal diameter of $0.9\,\mathrm{mm}$ in a distance of $2\,\mathrm{m}$ from the isolator. The isolator was therefore removed from the setup. Cubes made of borosilicate glass (BK7) also showed strong focusing effects, e.g. a $12\,\mathrm{mm}$ cube deformes a $2.5\,\mathrm{mm}$ collimated beam to a focused one with a focus of $1\,\mathrm{mm}$ and a focal length of $1\,\mathrm{m}$ when increasing the power as described above. That is why the setup is built completely without any cubes. Smaller effects produced by BK7 lenses could slightly be improved by choosing ones made of fused silica (SiO_2) at locations where the beam is small and power densities are high. Luckily, the TeO_2-crystals used in the AOMs showed nearly no thermal lensing effects. The slight astigmatism produced by the fact that the two axis of the crystal are not otically equal is nearly compensated by the fact that we use two perpendicular AOMs. However, the final step to overcome thermal lensing effects and produce a defined trap was to keep high power duty cycles short. In the current experimental cycle the laser operates at full power for less than $10\,\mathrm{ms}$ and is decreased to less than half this power within the first $100\,\mathrm{ms}$ of forced evaporation. This minimizes the heat transferred to the optical elements.

3.3.2 Performance

Key properties of the trap are the trap frequencies of the main axes, the heating rate and the particle loss rate. The first one is given by the size of the trap and the laser power. Heating rate and loss rate are mainly determined by the noise of the laser and the residual photon scattering rate in the trap.

The trap frequency are directly connected with the beam power and scale with $P \propto \sqrt{\omega}$. They can be measured by simply modulating the intensity of the laser power and thereby parametrically heat the trap. The number of atoms and the temperature after a defined number of kicks in dependence of this excitation frequency can be observed. When the frequency is equal to twice the trap frequency the atoms are heated and leave the trap. This is because the atoms get a kick in both turning points of their movement in the harmonic potential. Hence the energy of each kick adds up until the energy of the particle exceeds the trapping potential and it leaves the trap. Since the trap is not fully harmonic, but becomes anharmonic in the regions further away from the center of the Gaussian beam, the loss of atoms reaches its maximum at frequencies lower than the real trap frequency. This is because the anharmonic part of the potential shifts down the eigenfrequen-

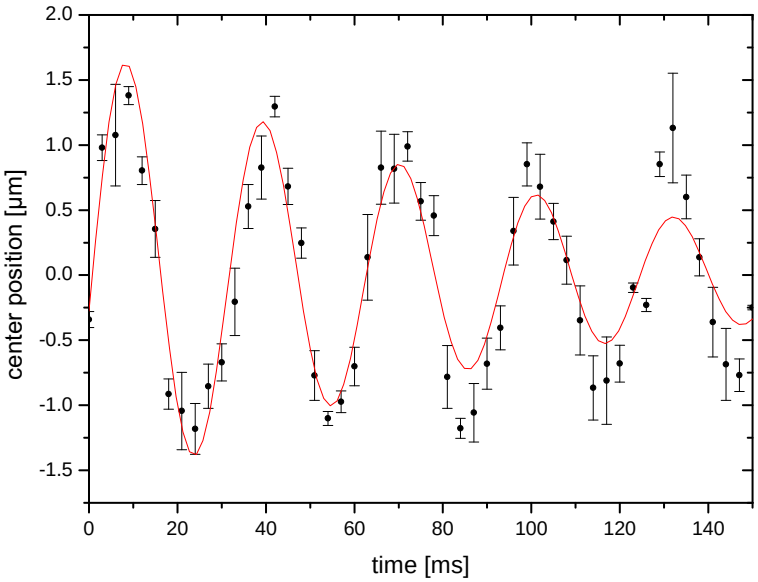

Figure 3.4: Measurement of the axial trap frequency at a laser power of $120\,\mathrm{mW}$. Ramping up the magnetic field for a few ms causes the atomic cloud to oscillate in the trap with the trap frequency. The fit shows a damped sine. The errors are the statistical errors of at least five independent measurements.

cies of the oscillator. A more precise indicator is therefore the temperature of the sample, obtained by a time-of-flight (TOF) measurement. For efficient heating of the whole atomic sample, the atoms have to be shaken without immediately leaving the trap. The temperature therefore reaches its maximum at the frequency at which the bottom of the trap is in resonance with the excitation frequency, that is the actual trap frequency. Figure 3.3 shows one example of such a measurement. Note that the temperature decreases slightly before it increases to the maximum value. This is also a consequence of the anharmonic part of the trap. Since the hottest particle with the highest energy are preferably in the anharmonic region, they are removed at lower frequency. Removing the hottest particle leads to a decrement of the total temperature. Figure 3.5 shows the obtained trap frequencies for our trap in dependence of the potential depth. The plotted error bars in the trap frequency measurement are the standard error from at least five independent measurements, the errors in the trap frequency graph are taken from the fit. The frequencies decrease with the square root of the laser power as expected.

A cross-check for the validity of this type of measurement is the excitation of dipole oscillation of the cloud. After evaporatively cooling the cloud to a certain

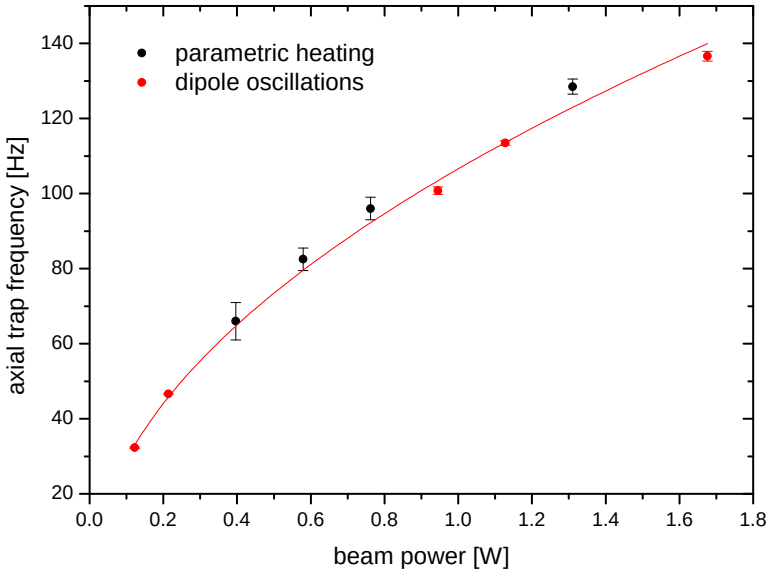

Figure 3.5: Axial trap frequency versus laser intensity. The red points were measured by exiting dipole oscillations, the black ones by parametric heating. The errors are the $95\,\%$ confidence interval of the fit to the respective measurement. All points lie within their error bars on the fitted square root function.

trap depth, the potential can be ramped up and an oscillation of the center of mass of the cloud in the trap with the trap frequency can be excited. For this purpose we make use of a magnetic field gradient in our trap, which excites such an oscillation when ramping up the magnetic field for a few ms. The damping of this oscillation is an indicator for the anharmonicity of the trap, since higher orders in the expansion of the trapping potential lead to a dephasing of the motion of the particles, blurring the oscillation of the cloud and damping it out. Figure 3.4 gives an example of such a measurement. Observing these oscillations in the slow axis of our trap, we can clearly see that both measurements lead to equal trap frequencies within the experimental errors. A comparison of a fit only to the points measured by exciting dipole oscillations and the ones measured by shaking the trap revealed a difference of 5% between both measurements. This seems a plausible value for the error of the trap frequencies.

Heating in a trap results from noise in the laser power, its pointing instability and from remaining photon scattering processes. Figure 3.6 shows the heating rate in the trap at different laser powers at a magnetic field of $561\,\mathrm{G}$, where we make our three component Fermi mixture. The evaporation was obtained down to a laser

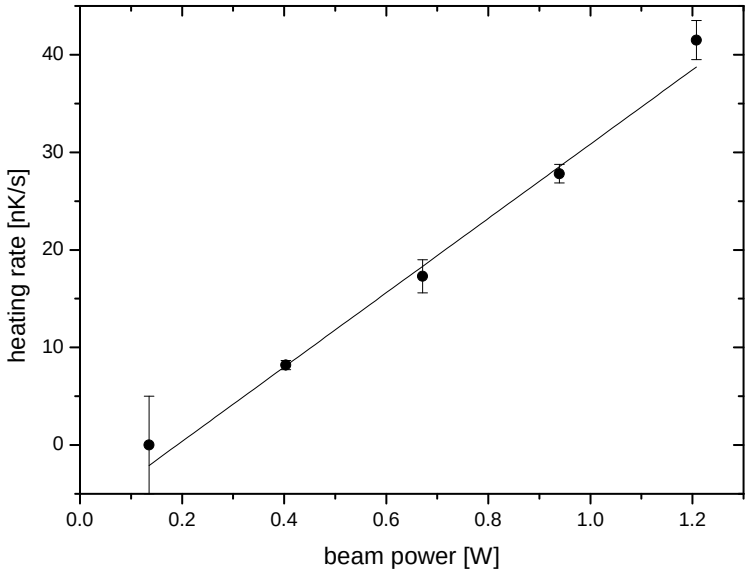

Figure 3.6: Heating rate of the trap measured in a fermionic sample. Each point originates from a fit to a lifetime measurement at the respective trap depth. The sample was evaporated to a depth of $135\,\mathrm{mW}$, then the trap was compressed up to the probe depth and the temperature was observed over $20\,\mathrm{s}$. The errors are the $95\,\%$ confidence interval of the fit parameters.

power of $135\,mW$ as explained in chapter 5. Then the magnetic field is switched to $561\,\mathrm{G}$ and the laser power is ramped up to the respective probe value. This has to be done slowly compared to the trap frequencies to minimalize heating by re-compression of the trap. However, the trap is heated adiabatically, proportional to the square root of the beam power. The particles of state $|2\rangle$ are removed from the trap with a resonant laser pulse to ensure that only single particle processes take part in the heating. Since identical fermions cannot scatter via s-wave scattering and therefore do not interact at low temperatures, the only possibility to deposit energy in the sample is by photon-atom interaction. The heating rates plotted in figure 3.6 are the result of a linear fit to the evolution of the temperature during the first $2\,\mathrm{s}$ after the laser power has reached the probe value.

A rough estimate of the heating induced by the scattering of photons can be obtained assuming that the atoms scatter photons with a rate of the peak scattering rate derived from equation 2.6. This is valid, since at a truncation parameter of 7.14 all of the atoms are close to the trap center. An upper limit for the heating rate can be derived by assuming that every particle remains in the trap and absorbs

the total energy of the scattered photons. This would lead to a heating rate of $k_B\dot{T} = \Gamma_{sc}(0)(\hbar k)^2/2m$, which yields a heating rate of $11.2\,\mathrm{nK/s}$ at a beam power of $400\,\mathrm{mW}$. Note that the heating drops to zero at a beam power of $0.2\,\mathrm{W}$ which corresponds to a trap depth in terms of temperature of $6\,\mu\mathrm{K}$. A single photon transfers an energy of $E_{rec} = (\hbar k)^2/m = 3\,\mu\mathrm{K}$ to the atoms. This is exactly half the potential depth. But since the atoms can leave the trap into the single beams forming the trap, the barrier for escaping is only half as high as the total trap depth. Hence all particles that scatter a photon leave the trap and cannot contribute to heating.

Of course, this model overestimates the real heating rate. Yet the fact that the measured heating rates are on the same order of magnitude as these results and the zero crossing is consistent with the recoil energy transfered in a single scattering process shows, that we are primarily limited by the remaining photon scattering. To achieve lower heating rates, a laser with a larger wavelength has to be used. This would reduce the energy of a single photon as well as the scattering rate. Since this would also lower the potential depth, the power would have to be increased to achieve the same experimental conditions.

3.4 Drawing time-averaged potentials

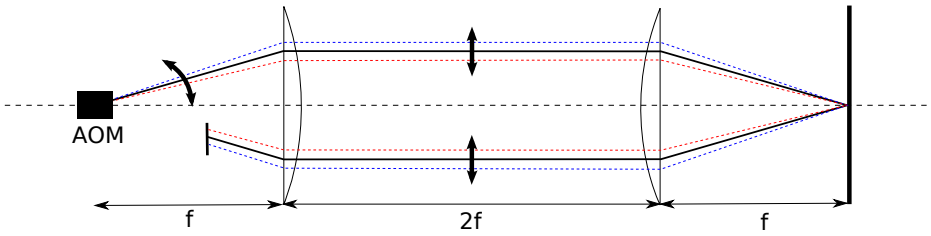

Figure 3.7: A lens transforms a change in the propagation angle into a change in position, if the AOM is set up in the focus of the lens. Deflection dimensions are exaggerated.

In an acousto-optic modulator (AOM), a beam traveling through a crystal is deflected by a sound wave in the crystal. The deviations in the optical density created by the sound wave produce a lattice at which the incoming beam undergoes Bragg diffraction. By varying the frequency of the sound wave, the diffraction angle of the diffracted beams can be influenced. Since momentum conservation has to be fulfilled, changing the frequency of the sound wave also changes the frequency of the transmitted beam. But since the dipole trap laser is very far detuned with respect to the atomic transition, in this case this effect can be neglected . We can

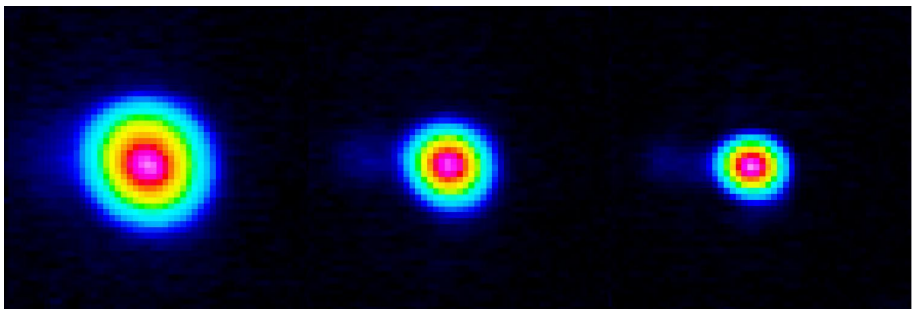

Figure 3.8: Beam camera images for different amplitudes of modulation. The beam diameter decreases from left to right from $200\,\mu\mathrm{m}$ to $100\,\mu\mathrm{m}$.

therefore use the possibility of changing the diffraction angle of the first diffraction order to "paint" a variety of potentials. "Painting" means here that the laser scans a certain area with a frequency much higher than the trap frequencies, so that the atoms are only influenced by the time-averaged potential. In detail this is done the following way:

The beam is transmitted through two AOMs, mounted perpendicular to each other. Assuming the z-axis in the direction of the beam propagation, the beam can be moved in the $x-y$-plane. Moving means here that the diffration angle of the AOM and therefore initially the angle of propagation can be changed. A lens set up in the distance of the focal length transforms the change in the propagation angle into a change in position. When the beam is reflected back into the chamber, the movement is mirrored at the optical axis as shown in 3.7. Therefore, moving the beam of a crossed dipole trap always leads to a symmetric time-averaged potential.

Since we can control the frequency of the sound wave using an arbitrary waveform generator (AWG) we can load waveforms at will into the memory of the AWG and accomplish movements in nearly any path of the x-y-plane within the limits of the AOM. However, the diffraction efficiency depends on the diffraction angle. It has to be taken into account that at regions further away from the center, the beam has to stay longer to transfer an equal amount of energy to that point. Figure 3.8 shows beam profiles produced by applying a spiral movement with different amplitudes to the AOM. The pictures were taken with a beam profile camera.

The first idea was to enlarge the trap for the transfer from the MOT to the dipole trap. Since the MOT covers a far larger volume than the dipole trap, it can be hoped that by enlarging the dipole trap the spatial overlap of both traps increases and more atoms can be transferred. During evaporation the trap is reduced to the actual focus of the trapping beam again. Figure 3.9 shows the number of transferred particles after the first step of evaporation, where trap sizes are equal

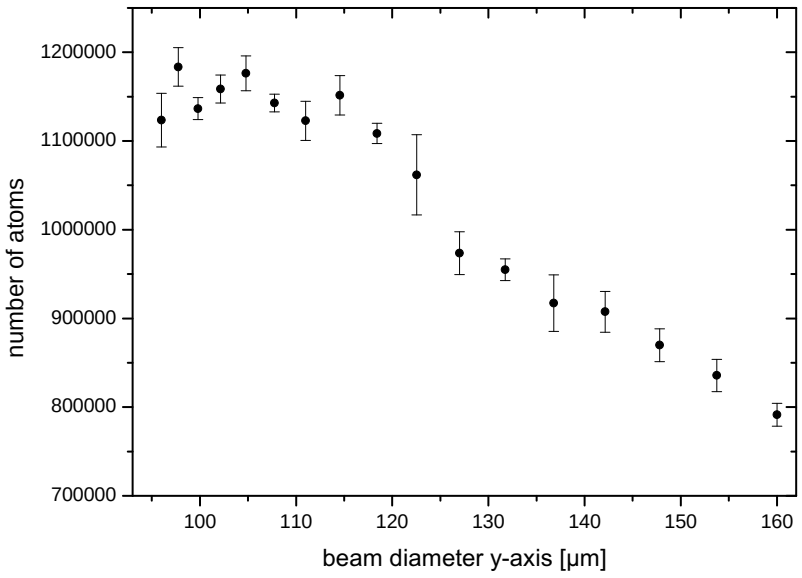

Figure 3.9: Number of atoms after first part of evaporation versus beam waist at transfer. The errors are the statistical errors of at least five independent measurements.

again. The trap was enlarged by changing the RF frequency of the vertical AOM in a sinusoidal way with a frequency of $200\,\mathrm{kHz}$. The x-axis gives the maximum size of the beam at transfer. Unfortunately, the overall transfer rate is neither reduced nor enlarged at small modulating amplitudes. At higher amplitudes the number of transferred atoms decreases, probably because the gain in spatial overlap of both traps is overcompensated by the flattening of the trap. Modulating the beam in both axis does not improve this problem.

However, we found that the properties of the trap can slightly be improved by modulating the beam at the end of evaporation. At small trap depth the particles are the most sensitive to the laser noise. Modulating the beam position a little bit might flatten the inhomogenities in the trapping potential, which possibly reduces heating or particle loss. Figure 3.10 shows the gain in particle number for a given expansion energy of the condensate when doing the final evaporation by enlarging the effective beam. It might be possible to get rid of the final loss shown in figure 4.2 using this method. But since this method also lowers the trap frequencies, a closer look at the phase space density has to be taken before judging which method is the better choice on the way towards a cold with low expansion energies.

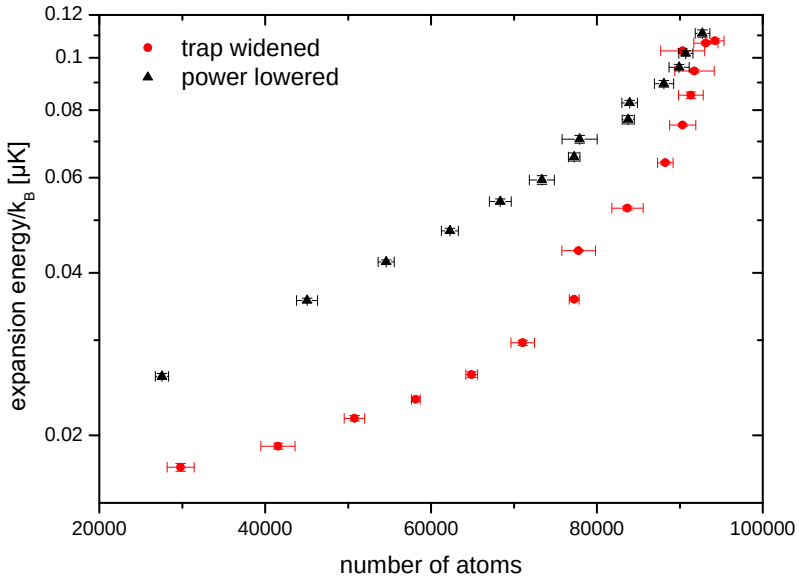

Figure 3.10: Final part of evaporation. The trap is lowered to a depth of $70\,\mathrm{mW}$ as described in chapter 4. For the black curve the beam power was simply lowered further down to different trap values. After $1s$ plain evaporation the expansion energy and the number of atoms of the sample were measured in a time of flight measurement. For the red curve the trap was widened to different sizes and the same measurements were performed.

3.5 Magnetic field

3.5.1 Feshbach coils

The interaction between the particles can simply be tuned by applying a magnetic field as shown in section 2.2. This field is provided by two coils in Helmholtz configuration around the center of the octagon, called Feshbach coils. To access the full resonant region, these coils have to provide a homogeneous field of up to $1500\,\mathrm{G}$ at the point where the atoms are trapped. The design of these coils is one of the great challenges in the setup of our experiment.

In principle, there are two posibilities to construct these coils: Either the coils can be placed far away from the trap with sufficient space for large coils and a complex cooling system. Or small coils can be produced and brought close to the atomic cloud. However, this raises the problem that the space for cooling equipment is rather limited. Although these coils would need less power, it is a challenge to

dissipate the produced heat from the coils and avoid destruction.

The vacuum chamber has an inset for the Feshbach coils at the reentrant viewport. This allows to bring the coils to a distance of $31\,\mathrm{mm}$. At the same time it limits the inner diameter of the coil to $58\,\mathrm{mm}$ and fixes the outer diameter to $96\,\mathrm{mm}$. The coils consists of a copper wire of $1\,\mathrm{mm} \times 5\,\mathrm{mm}$. To get a sufficient amount of windings for a homogeneous field, the width of the wire was chosen small. In contrast, the length was chosen larger to increase the area conducting the current. This reduces the resistance of the wire and with that the heat produced in the coils. The choosen extensions allow for the creation of coils with 15 windings, requiring $400\,\mathrm{A}$ to produce a field of $1500\,\mathrm{G}$ in the given configuration. The resistance of the coils was measured to be $\approx 13\,\mathrm{m}\Omega$, which results a power deposited in the coils of $P = RI^2 = 2000\,\mathrm{W}$.

The great challenge is now to dissipate the heat from the coils. Therefore, they are glued to a heat sink made of copper. The critical point in the cooling process is the transport of the heat from the wire to the sink. Since the isolation of the copper wire is a bad thermal conductor, the upper side of the coils was abraded before being glued to the sink. For the first generation of coils we used a filled epoxy (Emerson and Cuming, Stycast 2762FT) with a thermal conductivity of $1.34\,\mathrm{W/mK}$. These coils have a maximal continuous operation current of about $210\,\mathrm{A}$. At this current the maximal temperature of the coils reaches up to $100\,^{\circ}\mathrm{C}$, a temperature that should not be exceeded too much, since the glue of the coils as well as the octagon itself could suffer critical damage. The coils can be driven with $400\,\mathrm{A}$ for a few $100\,\mathrm{ms}$. These operation properties are sufficient for the experiment, since the magnetic field for evaporation can be produced continuously, while for experiments in the high field regime the provided time is sufficient.

However, we found that the performance of the coils decreases with time. Roughly half a year after the coils were put into operation, the highest temperature of the coils at continuous operation with $210\,\mathrm{A}$ raised to about $160\,^{\circ}\mathrm{C}$. This might be caused by degradation of the thermal connection between coil and sink, because the porous Stycast cannot cope with the mechanical stress during many experimental cycles. This forces us to build a second generation of coils, employing diamond filled Epoxy (AI technology, Prima-Bond ME7159), with a thermal conductivity of $11.4\,\mathrm{W/mK}$. This Epoxy showed promising properties when trying to repair the existing coils and will hopefully work even better in the new set of coils.

3.5.2 Switching polarity

In order to get a homogeneous magnetic field at the center of the trap, it is important that the atomic cloud is in the exact center of the magnetic field created by the Feshbach coils. To rule out any misalignment the coils creating the MOT-field

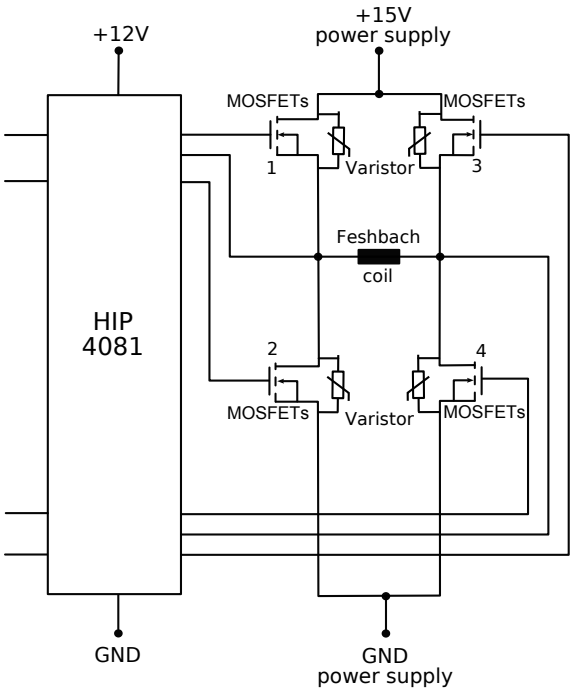

Figure 3.11: Circuit diagram for the H-bridge changing the polarization of the Feshbach coils.

are switched off and the field is taken over by the Feshbach coils shortly before the atoms are transferred into the dipole trap. Since the MOT needs a quadrupole field that is created by two coils in Anti-Helmholtz configuration, it must be possible to switch the polarity of at least one of the coils. To avoid particle loss and heating, this has to be done at a time scale of about $1\,\mathrm{ms}$. Switching is done by a so-called H-bridge presented in figure 3.11. Via four MOSFETs the supply lines of the coil can be connected either to the positive potential of the power supply or to ground. The two possibilities to operate the coil are to open MOSFET 1 and 4 or 2 and 3 and close the other two. To switch off the coil, gates 2 and 4 or 1 and 3 have to be opened. In every case it must be avoided to open 1 and 2 or 3 and 4 at the same time, because this would lead to a short circuit which could destroy the setup. The MOSFETs can also be destroyed by only partly opening their gates. If the resistance of the MOSFETs increases, the current of up to $400A$ will immediately overheat the device. Luckily there are ICs available, which take care of these problems. The HIP4081a automatically avoids short circuits and intermediate voltage at the gates. Apart from these logic elements, the HIP is essentially a charge pump, which pumps the charge from external capacitors to the gates of the MOSFETs in the moment of switching. This allows the HIP to be independent of absolute voltages and to hold the potential difference between the three pairs of

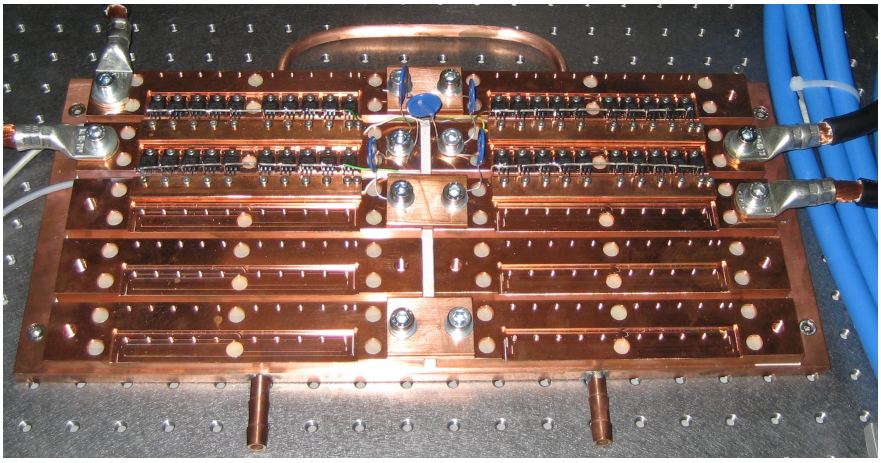

Figure 3.12: Picture of the MOSFET bench for switching the polarity of the coils.

the six outputs constant. The two connection possibilities on each side of the core can be switched very conveniently with a TTL signal.

The MOSFETs have to switch up to $400\,\mathrm{A}$. In the normal design of these components the maximum current is limited by the current their connectors can conduct. The connectors can only safely be driven with a current of less then $80\,\mathrm{A}$. This leaves the possibility to switch to more expensive devices or to connect many MOSFETs in parallel. As the second alternative is cheaper and in the case of failure more convenient to repair, we decided to put 10 MOSFETs (IRFB3077) for each switching point in parallel. The MOSFETs are screwed onto a copper bench which can dissipate the produced heat (see figure 3.12). The resistance of the MOSFETs between source and drain is about $3\,\mathrm{m\Omega}$. At a current of $200\,\mathrm{A}$ this results a power of $P = RI^2 = 1.2\,\mathrm{W}$ per MOSFET. Of course, the whole setup is oversized for the dissipation of this power . Yet since the power increases quadratically with the current and for high fields the MOSFETs have to switch twice the current, we are sure that everything will keep working, even if single MOSFETs are destroyed. Another advantage of this system is that MOSFETs that are not working anymore can be replaced very easily. The bench is capable of up to 80 MOSFETs to switch the polarity of both coils. This can be used to ramp down the magnetic field very fast by changing the polarity of both coils. It reduces induced currents and accelerates the decay of the magnetic field. Since for current experiments this is not necessary yet, there are only 40 MOSFETs implemented to switch one coil at the transfer.

To make sure that the MOSFETs are not destroyed by induction voltage, there are varistors connected in parallel to the MOSFETs. These devices work like voltage dependent resistors which direct the current around the MOSFETs if the voltage

exceeds the normal operating voltage.

3.5.3 Stabilization and calibration

The magnetic field is stabilized with a $100\,\mathrm{kHz}$ digital PID loop implemented in our experiment control. The current running through the coils is first transformed with a current transducer (Danfysik, Ultrastab866-600) with a ratio of $1500:1$ and then transformed into a voltage by a high precision resistor (ISA-Plan type A-H, Isabellenhütte). This voltage is amplified by a factor of three by an operational amplifier to fit the full range of the input of our experimental control. The remaining noise on the current is in the order of 10^{-4} RMS, corresponding to a field stability of $\pm 50\,\mathrm{mG}$ at a magnetic field of $500\,\mathrm{G}$. The input has a resolution of $16\,\mathrm{bit}$ for $\pm 10\,\mathrm{V}$, which corresponds to a step size of $0.3\,\mathrm{mV}$ or $53\,\mathrm{mG}$ per bit. This limits the control of the magnetic field, because the flipping of a single bit on the control signal can be observed. Extending the input to $18\,\mathrm{bit}$ will increase the magnetic field resolution by a factor of four and offers the possibility of more precise experiments.

The calibration of the magnetic field is done by driving transitions between the lowest hyperfine states. Since the desired frequency of the RF field is extremely sensitive to the magnetic field, this gives a sufficient calibration. For instance, the number of particles in state $|1\rangle$ can be observed while scanning the frequency around a roughly estimated transition. From the frequency where maximal loss from state $|1\rangle$ is observed, the related magnetic field can be calculated. The transition frequency scales with $16\,\mathrm{kHz/G}$ at a field of $300\,\mathrm{G}$. This means that we are able to calibrate the magnetic field with higher precision than the setup allows to control the field.

3.6 RF setup

To induce a transition between the three lowest hyperfine states, a RF field according to the energy differences of these states has to be applied to the sample. The energy differences and therefore the required frequencies scale with the magnetic field. At the field applied in our setup the desired frequencies vary between $70 - 85\,\mathrm{MHz}$, which corresponds to wavelengths of about $\approx 4\,\mathrm{m}$. The field is produced by an antenna connected to a RF generator setup. Since the distance between the antenna and the center of the trap is much smaller than the wavelength, the point where the field is required lies in the near field range of the antenna and the antenna does not have to send electromagnetic waves. A simple and effective setup is to use a wire antenna. The wire is turned to a circle fitting around the MOT beam at the reentrant viewport. The impedance of the antenna has to be

matched to the impedance of the amplifier output to avoid backreflection of the RF signal at the connector. This is done by a capacitor that is connected parallel to the antenna. The other value that has to be adjusted is the resonance frequency of the oscillating circuit composed by the inductance and the capacity of the wire. This is done by connecting a capacitor in series with the antenna. This maximizes the current in the antenna and therefore the field at the center of the trap. In the current setup the antenna is designed to be in resonance at a frequency of $80\,\mathrm{MHz}$.

The RF is needed to create a balanced mixture between the three lowest hyperfine states of $^6\mathrm{Li}$. The $|1\rangle \leftrightarrow |3\rangle$ transition is forbidden in first order due to angular momentum conservation, so only the transitions $|1\rangle \leftrightarrow |2\rangle$ and $|2\rangle \leftrightarrow |3\rangle$ can be driven. Therefore, we need to apply two RF frequencies simultaneously to the atomic sample. The two frequencies can be produced by mixing the center frequency with a frequency equal to half of the frequency difference. Mixing both signals yields frequencies at the desired amount, since mixing two sinusoidal signals always produces the sum and the difference frequency of the two separate signals.

The only device able to produce a frequency higher than $80\,\mathrm{MHz}$ in our lab is a $6\,\mathrm{GHz}$ spectrum analyzer (Rhode und Schwarz FSL) with a generator output, which can be controlled via our experiment control. The spectrum analyzer is used to produce the center frequency. The much lower difference frequency is taken from an arbitrary waveform generator (AWG) (Stanford Research DS345) and mixed with the signal from the spectrum analyser.

During the inital evaporation a slight imbalance between states $|1\rangle$ and $|2\rangle$ is removed with the RF signal from another AWG (Agilent 33250 A). Its output is fed through a frequency doubler to reach the desired frequency. A switch allows to choose between the two signals and also makes it possible to turn off the RF completely. After the switch the signal is send through a $5\,\mathrm{W}$ amplifier, whose output is connected to the antenna. The antenna is set up at the lower reentrant viewport, as close to the atomic sample as possible. It produces an AC field from the RF signal to drive the atomic transitions. A new amplifier with an output power of $100\,\mathrm{W}$ is already bought and will soon be implemented into the setup. The gain in power by a factor of 20 will simplify and accelerate driving RF transitions. Small disalignments between the magnetic field and the RF frequency will be compensated by the high power.

Chapter 4

Creation of a molecular BEC

4.1 Motivation

With the creation of a molecular BEC our apparatus catches up to the state of the art in the field of ultracold quantum gases. Since our first BEC in February 2008 we have reproduced a number of milestones in experiments with ultracold fermions. By doing this, we have learned how our apparatus works and are ready to go for new physics.

On our way towards a finite degenerate Fermi gas, with the creation of a molecular BEC we have reached the point, where we can also create a degenerate Fermi gas. By simply ramping the magnetic field over the Feshbach resonance, the bosonic molecules can be transformed into fermions. Since the bosons are degenerate and the crossing of the resonance is isentropic, also the fermions will be degenerate. There are also ways to cool fermions directly. Yet there are some major problems: Since cooling in these samples is obtained by evaporation, scattering is a vital process to reach ultracold temperatures. Because s-wave scattering is forbidden for identical fermions, scattering nearly vanishes at low temperatures. In order to reach degeneracy a second particle species has to be added. We chose the experimentally most simple option, which is to trap two different hyperfine states. However, even with two different fermions, scattering starts to be suppressed when degeneracy sets in. Due to Pauli blocking only fermions at the Fermi edge can find free momentum states in their vincinity and therefore change their momentum in s-wave collisions. Forming molecules from the fermions circumvents all these problems and leads directly to a deeply degenerate Fermi gas.

4.2 Evaporation

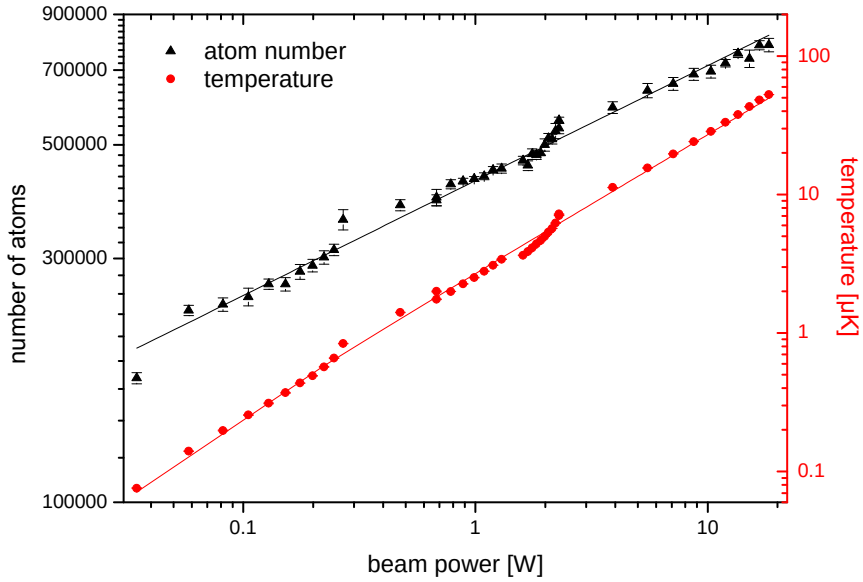

Figure 4.1: Evaluation of the number of particles and their temperature during PID loop evaporation for a molecular BEC. The errorbars are the statistical errors of at least five independent measurements. The fit to the number of atoms is done with the model given in equation 2.10. It results $\eta = 8.88(2)$. The fit to the temperature is a linear one with a slope of $2.71(1)\,\mu\mathrm{K/W}$, which corresponds to $\eta = 11.3(1)$. The errors are taken from the fit and certainly underestimate the real errors.

At an oven temperature of $350\,^{\circ}\mathrm{C}$ our MOT loads about 2×10^8 atoms in $1\,\mathrm{s}$. The particles are transferred into the dipole trap and cooled towards a BEC in the following experimental cycle:

About $90\,\mathrm{ms}$ before the transfer, the MOT coils are switched off and the quadrupole field is produced by the Feshbach coils. This is done to position the atomic cloud in the exact center of the homogeneous field produced by the Feshbach coils, circumventing any possible misalignment of the coils. $10\,\mathrm{ms}$ before the transfer the laser intensity in the MOT beams is lowered while at the same time the detuning of the laser approaches resonance to compress and cool the trap for the transfer. $5\,\mathrm{ms}$ before the transfer the power of the dipole laser starts to increase, taking $3\,\mathrm{ms}$ to reach its full power of $130\,\mathrm{W}$ in the trap. In the moment of the transfer the cooler and the repumper laser are switched off, the polarity of the Feshbach coils is

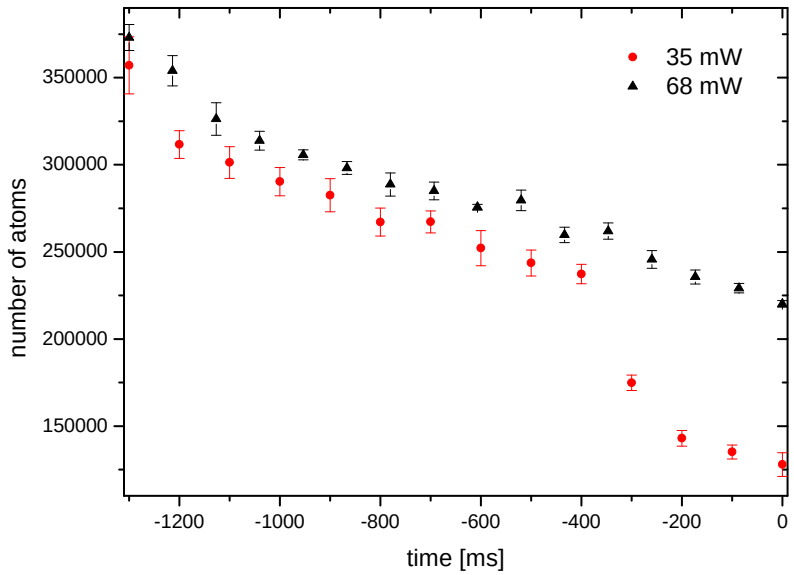

Figure 4.2: Evolution of the number of particles during the last ramp of evaporation and $300\,\mathrm{ms}$ plain evaporation. The time scale is counted from the end of evaporation. Before plain evaporation there is a ramp of $1000\,\mathrm{ms}$ from $270\,\mathrm{mW}$ to $35\,\mathrm{mW}$ (red curve) and to $68\,\mathrm{mW}$ (black curve). The curves reveal a loss at low trap depth, probably induced by a magnetic field gradient. The errorbars are the statistical errors of at least five independent measurements.

switched to produce a homogeneous field and the current of the coils is turned up to create a field of $751\,\mathrm{G}$ and so tuning the scattering length to a value of $3500\,a_0$, where fast and efficient evaporation is possible. The repumper is switched off slightly before the cooler, ensuring that all atoms are transferred to the dipole trap in the $F = 1/2$ state.

$5\,\mathrm{ms}$ after the transfer, forced evaporation starts. At first the laser power is lowered by simply employing the external control input of the laser and so ramping down the beam power from $130\,\mathrm{W}$ to $50\,\mathrm{W}$ in $150\,\mathrm{ms}$ and then further from $50\,\mathrm{W}$ to $22\,\mathrm{W}$ within $400\,\mathrm{ms}$.

The second part of the evaporation is done by lowering the laser power using the vertical AOM. The power transmitted through the AOM is monitored by a photo diode and can therefore be stabilized using a digital PID loop implemented into our experimental control. This way we execute two ramps employing a SI-diode, one from $12.9\,\mathrm{W} \rightarrow 2.29\,\mathrm{W}$ in $500\,\mathrm{ms}$ and one from $2.29\,\mathrm{W} \rightarrow 1.25\,\mathrm{W}$ in another $500\,\mathrm{ms}$. For the last ramp we employ a GaAs-diode to improve signal-to-

noise ratios at low intensities and finally ramp down the laser power to $34.8\,\mathrm{mW}$ in $1200\,\mathrm{ms}$, followed by $300\,\mathrm{ms}$ plain evaporation.

Figure 4.1 shows the measured number of particles at different stages of evaporation. $10\,\mathrm{ms}$ before the atoms are released for the time-of-flight measurement the magnetic field is ramped up to $786\,\mathrm{G}$. At this field the binding energy is reduced to $E_{\mathrm{bin}}/k_B = 500\mathrm{nK}$ and the molecules can be imaged with resonant light. Note that for different temperatures the time-of-flight had to be adjusted to get reliable data. The absorption imaging has large errors if the cloud is too dilute and signal-to-noise ratio is bad. If the cloud is too dense the absorption becomes saturated which also leads to false values. This is why the estimated number of atoms differs from the linear fit at the end and at the beginning of each measurement. The fit to the number of atoms is evaluated according to the model given in equation 2.10 and results $\eta = 8.88(2)$. The linear fit to the temperature versus beam power is much more direct since the inverse of the slope is proportional to η. The conversion factor however depends quadratically on the beam waist at the center of the trap (compare equation 2.7). Since the focus in the vacuum chamber cannot be observed directly, the uncertainty of this value also leads to an uncertainty in the conversion factor. Those systematic errors from the experiment are large compared to the ones obtained from the fit. The difference between both η shows, that a number of particles is lost during evaporation due to residual heating. However, the estimated value is quite rough, since it depends strongly on the chosen start values U_0 and N_0 for the fit. Those uncertainties lead to an an error in the order of at least 10%.

In general, the values resulting for η are quite good, but still there is room for improvement. Since the improvement would have to lead to much longer experimental cycles and the number of particles at the end of evaporation would only increase slightly, we chose this trade-off between efficiency and speed. The number of particles at the end of the last ramp is sufficient for the planned experiments.

4.3 Creation of molecules

When the temperature of the particles decreases further and further, their kinetic energy originating from their thermal motion comes into the same order of magnitude as the binding energy of a stable molecule and molecule formation sets in. The fraction of atoms bound in molecules at a certain temperature in thermal equilibrium can be calculated as $\exp(-k_B T/E_B)$, with E_B the binding energy of the molecule. At a magnetic field of $751\,\mathrm{G}$ the scattering length for the $|1\rangle \leftrightarrow |2\rangle$ mixture is $3560\,a_0$, which yields a binding energy in terms of temperature of $E_B/k_B = \hbar^2/(ma^2 k_B) \approx 2.2\,\mu\mathrm{K}$.

The process of molecule formation can be measured in two different ways: The

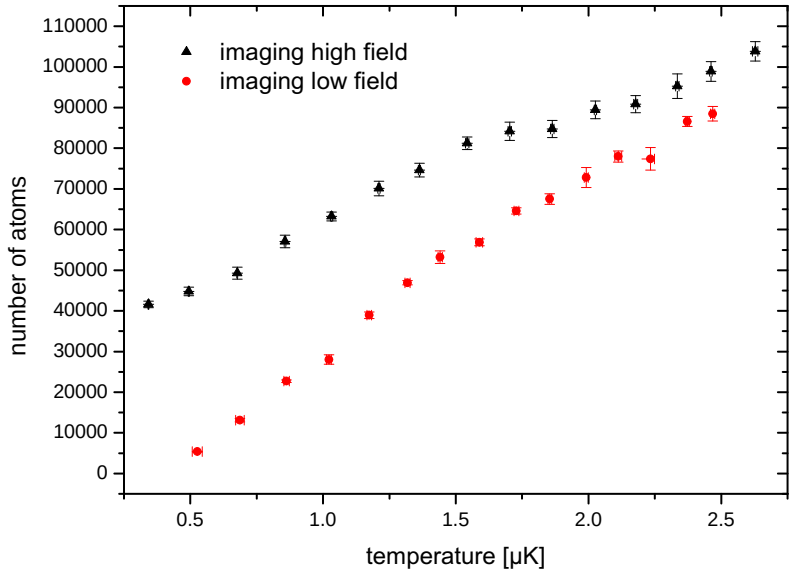

Figure 4.3: Molecule formation during evaporation. The red curve shows the number of atom measured at a field of $560\,\mathrm{G}$, where the atoms bound in molecules are not in resonance with the imaging beam. For the black curve the field was ramped up to $786\,\mathrm{G}$, where the binding energy is low and quasi-free atoms can be imaged. The errorbars are the statistical errors of at least five independent measurements.

first one makes use of the fact that in a bound state the atomic transitions are shifted. That means that they cannot be imaged with light resonant to the transition of a free atom. Figure 4.3 shows two curves. For the red one the atoms are imaged at a field of $560\,\mathrm{G}$. For the black one the measurement is done at a field of $786\,\mathrm{G}$. The evaporation is done as described in section 4.2 and the field is afterwards ramped to $560\,\mathrm{G}$. Because the binding energy increases with decreasing magnetic field, molecular relaxation becomes more likely to lead to a loss from the trap. To be sure that this loss is not taken into account when measuring the difference between molecules and atoms, for both measurements the field is decreased $15\,\mathrm{ms}$ before the image is taken. For the red curve the picture is taken at this field, and for the black one the field is ramped up to $786\,\mathrm{G}$ $4\,\mathrm{ms}$ before the imaging. Trying to ramp the field closer to the moment of imaging yields a decrement of the number of atoms, indicating that the field has not yet reached its final value and the atomic transition is not in resonance with the absorption beam. Since the binding energy scales with the inverse square of the scattering length, the binding energy

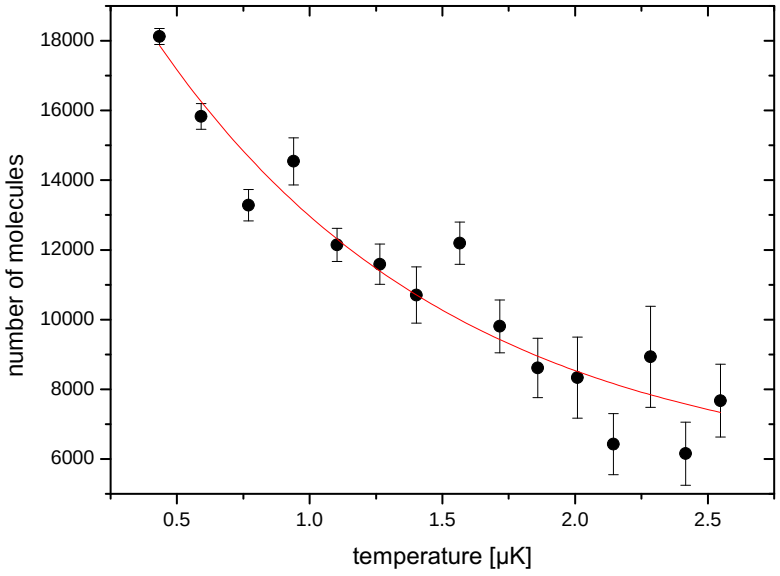

Figure 4.4: Number of molecules over temperature obtained from the difference of the two curves from figure 4.3. The fit is an exponential function, resulting a binding energy of $1.13\,\mu$K.

dramatically decreases when approaching the resonance. At a magnetic field of $786\,$G the binding energy of the molecules is small enough that they constituents can be imaged as quasi-free particles. The difference between the two measured values is close to twice the number of formed molecules as plotted in figure 4.4. The fit gives a binding energy of $1.1\,\mu$K. The underestimation of the molecule number rises from the fact that the cross section of the molecules and the light is not zero, even though the light is not in resonance with the molecule transition. Therefore, a number of photons is also scattered by the molecules but counted for atoms.

Another way to show the formation of molecules employs RF spectroscopy as shown in figure 4.5. After evaporation down to a certain potential depth a RF pulse is applied to the atomic sample. If the frequency of the signal matches the atomic transition $|2\rangle \leftrightarrow |3\rangle$, the atoms will flip their spin and become invisible for the imaging done with light resonant for the atoms in state $|2\rangle$. If the atoms are bound in molecules, the energy from the RF photon must be able to break the molecules before flipping the spin. The loss peak in the number of atoms for atoms bound in molecules is therefore detected at energies slightly higher: In the first graph of figure 4.5, the loss peak is at the atomic transition frequency. Cool-

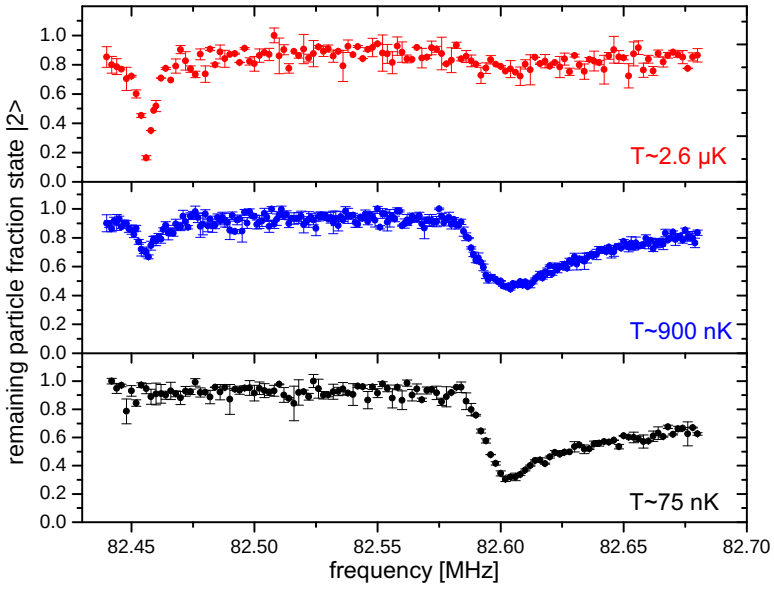

Figure 4.5: RF spectroscopy of an atomic sample at different temperatures. The left dip is produced by atoms in resonance with the RF field, the right one is shifted by the binding energy of the molecules, since the atoms have to be released before the spin can be flipped. The errorbars are the statistical errors of at least five independent measurements.

ing down further leads to the creation of molecules and a second peak appears. This peak rises from atoms bound in molecules. In the third graph, nearly all atoms have formed molecules. The shape of the molecule peak reflects the momentum distribution of the atoms in the molecule. It is the Fourier transform of the molecul wave function. The distance between the two peaks of $\approx$ 150 kHz allows to estimate a binding energy of $E_B \approx 600\,\mathrm{peV} \mathrel{\widehat{=}} 7\,\mu\mathrm{K}$. This agrees with the expectations for spectroscopy at a magnetic field of 720 G, where $a = 2180 a_0$. This is no surprise, since the scattering lengths were determined this way [22] and the agreement only shows that our apparatus works within the expected resolution.

4.4 Condensation

Further cooling leads to the condensation of Feshbach molecules into a BEC. In an absorption image this can be observed by a bimodal distribution arising from the thermal part and the condensate part at temperatures slightly below the critical

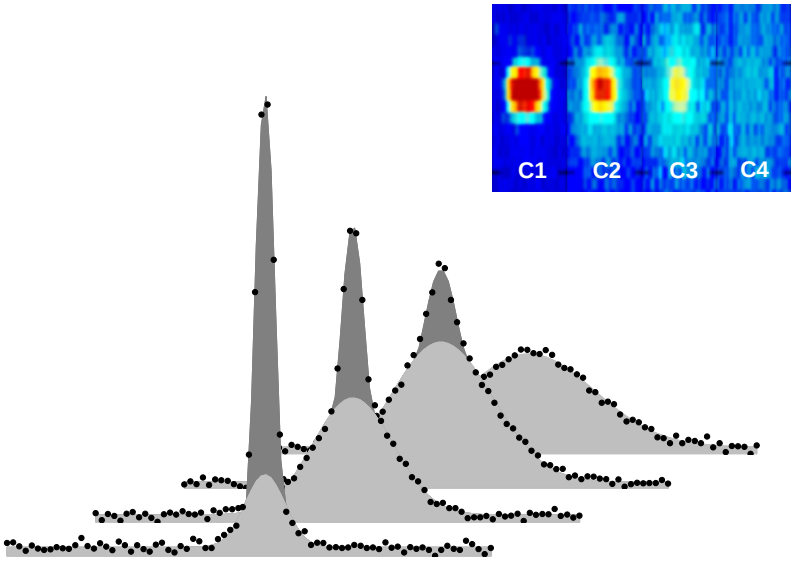

Figure 4.6: Bimodal distribution close to the critical temperature T_C. The lower images are the twice integrated density distributions after $10\,\mathrm{ms}$ TOF, the upper ones are false color absorption images taken by a CCD camera. The x-axis of the density distribution corresponds to the long axis of the absortion image and extends over $670\,\mu\mathrm{m}$.

temperature. Since the mean field energy is very large at $751\,\mathrm{G}$, the expansion of the condensate is on the same order of magnitude as the expansion of the thermal part. This makes it difficult to distinguish between both parts after a time-of-flight measurement. However, a little trick makes things easier: Directly after the trap is switched off for a time-of-flight measurement, the magnetic field is ramped to $500\,\mathrm{G}$, decreasing the meanfield energy and with that the expansion velocity of the BEC. Then the field is ramped up again to $785\,\mathrm{G}$ for imaging. This decreases the binding energy of the molecules as far that single atoms can be imaged.

Figure 4.6 illustrates the process of condensation. The absorption images in the lower part show that the peak density dramatically increases from the right one at high temperatures to the left one taken at much lower temperatures. Integrating over the radial axis leads to the curves shown in the upper part of the figure. This data is used to execute a bimodal fit. The fit is simply an inverted parabola added to a Gaussian, neglecting all interaction effects. The diluteness of the thermal cloud motivates such a neglection, and the quality of the fit (adjusted $\mathrm{R}^2 = 0.997$ for the bimodal distributions) proves the correctness of the assumption. The pa-

Property	Cloud C1	Cloud C2	Cloud C3	Cloud C4
Beam Power [mW]	35(2)	61(2)	99(3)	189(6)
Radial trap freq. [Hz]	194(10)	277(14)	367(19)	519(26)
Axial trap freq. [Hz]	19(1)	26(2)	34(2)	48(3)
Number of particles [$\times 10^3$]	55(1)	76(2)	99(2)	75(3)
Temperature [nK]	28(2)	115(1)	189(2)	309(3)
Condensate fraction	0.68(3)	0.24(1)	0.10(1)	0.002(2)

Table 4.1: Properties of the atomic clouds shown in figure 4.6

rameters of the fit are the physical values: condensate fraction f_{BEC}, width of the BEC w_{BEC} (determined by the meanfield energy), width of the thermal cloud w_{th} (proportional to the temperature) and total area A_{tot} (proportional to the number of particles) plus a center x_c and integration offset y_0. The normalization condition for the total area yields the amplitudes of the Gaussian and of the parabola:

$$A_{Gauss} = \frac{1 - f_{BEC}}{\sqrt{2\pi} w_{th}} A_{tot} \tag{4.1}$$

$$A_{BEC} = \frac{15}{16 w_{BEC}} f_{BEC} A_{tot} \,. \tag{4.2}$$

Using these values the fitted function is given as:

$$y = A_{Gauss} \exp\left(-\frac{(x - x_c)^2}{2w_{th}^2}\right) + A_{BEC}\left(1 - \left(\frac{x - x_c}{w_{BEC}}\right)^2\right)^2 \tag{4.3}$$

where the second part of the sum is only applied for $x_c - w_{BEC} < x < x_c + w_{BEC}$. It is important to choose the initial values for the fit carefully, because the convergence of the fit strongly depends on the starting conditions. Luckily, good initial parameters can be obtained from simply guessing them from the plotted graph. It is also possible to calculate the values using the considerations of chapter 2, but since the image is not taken in the trap but after a certain time-of-flight, it is not straight forward to do so. The case becomes even more complicated by the fact that during the expansion the interaction is tuned in a not exactly known way. Another reason why the formulas for the non-interacting case become senseless is that the scattering length in the condensate is in the order of a few thousand Bohr radii. A short calculation concerning a model presented in [25] showed that the estimated values differ from the non-interacting case by about $20\,\%$. Since this model is only valid for small deviations, even these approximations are not sufficient for our case. A detailed analysis of the behavior of the gas in such a

strong interacting regime is very difficult. But since the findings would not lead to great insights here, only the parameters obtained directly from the fit are given in table 4.1. The values and their errors for temperature, number of particles and condensate fraction are estimated from the fitted values. The error for the beam power of $3\,\%$ is the specified error of the thermal head of the power meter, since the error rising from the linear fit to the calibration measurements is an order of magnitude lower. It is noticeable that the number of particles for the highest temperature is lower than for the two lower temperatures. But as the absorption images show, several atoms have left the region of interest during time-of-flight and are not counted when summing up. The region of interest was chosen small in the direction of integration to increase signal-to-noise ratio. The less space with no significant signal is considered in the integration the less noise is added up.

4.5 BEC of $|1\rangle - |3\rangle$ molecules

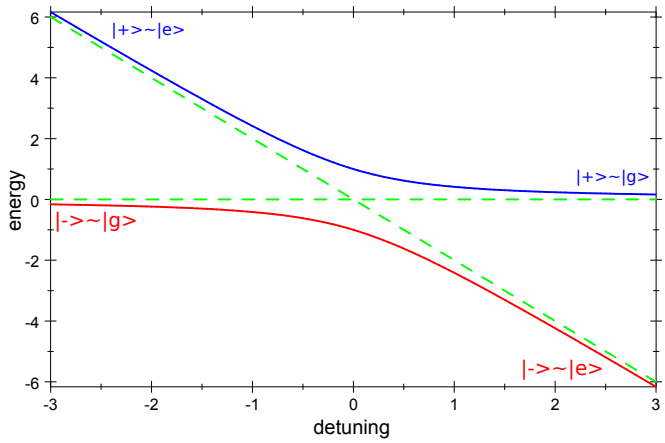

Figure 4.7: Avoided crossing around a resonance in an adiabatic passage.

Via driving RF transitions between state $|2\rangle$ and state $|3\rangle$ we can create a condensate from molecules of atoms in states $|1\rangle$ and $|3\rangle$. The sequence of the production also shows that ramping over the resonance does not affect the codensate: After the evaporation as described in section 4.2, the magnetic field is slowly increased from $751\,\mathrm{G}$ to $894\,\mathrm{G}$ in $100\,\mathrm{ms}$. Along the way the resonance is crossed and the BCS side of the resonance is reached. This means that the molecules transform into weakly bound Cooper pairs.

The free atoms of state $|2\rangle$ are transformed into state $|3\rangle$ in an adiabatic passage. In general, an adiabatic passage is a possibility to transform all particles from a certain ground state $|g\rangle$ into an exited state $|e\rangle$ when crossing a resonance. This

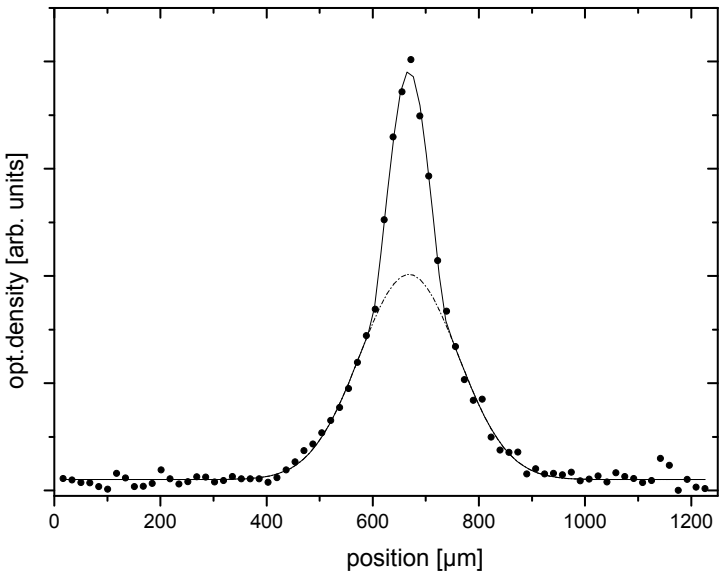

Figure 4.8: Bimodal distribution revealing a condensate of molecules formed by atoms in states $|1\rangle$ and $|3\rangle$.

is possible, because the eigenstates of the Hamiltonian of an atom in an external field are no longer the eigenstates of the atoms, but two new eigenstates $|+\rangle$ and $|-\rangle$, so-called dressed states. These eigenstates are a combination of the two atomic eigenstates and their contribution depends on the detuning δ of the external field relative to the atomic transition [29]. Figure 4.7 shows the behavior of the eigenstates of the Hamiltonian when crossing the resonance. Calculations show that at large negative detuning the $|-\rangle$ eigenstate is equal to the ground state $|g\rangle$. On the other side of the resonance, at large positive detuning the state $|-\rangle$ is approximately equal to $|e\rangle$. Since the $|-\rangle$ state is an eigenstate of the Hamiltonian of the system the atoms will stay in this eigenstate, if the detuning is not changed too fast. This way all atoms of the ground state will end up in the excited state when the frequency of the external field adiabatically crosses the resonance.

In our concrete case the ground state is an atom in state $|2\rangle$ and the exicted state is an atom in state $|3\rangle$. In the current setup it is not possible to slowly vary the frequency during an experimental cycle. So we keep the RF frequency fixed and vary the magnetic field. Due to the Zeeman effect the transition energy between the two states get shifted. This way we do not bring the external field into resonance with the transition but the transition into resonance with the external field.

In the experiment this is done by applying an RF field resonant to the $|2\rangle \leftrightarrow |3\rangle$

transition at approximately $897\mathrm{G}$ for $3\,\mathrm{ms}$ while ramping the magnetic field from $894\,\mathrm{G}$ to $900\,\mathrm{G}$. Thereafter nearly all the atoms in state $|2\rangle$ end up in state $|3\rangle$. The magnetic field is then ramped down to $666\,\mathrm{G}$, crossing the $|1\rangle - |3\rangle$ resonance. The final value is close to the resonance on the BEC side. Stable molecules are formed and condense into a BEC. Figure 4.8 shows a bimodal distribution at a temperature slightly below the critical temperature, obtained as described in section 4.4.

4.6 Crossover to the BCS regime

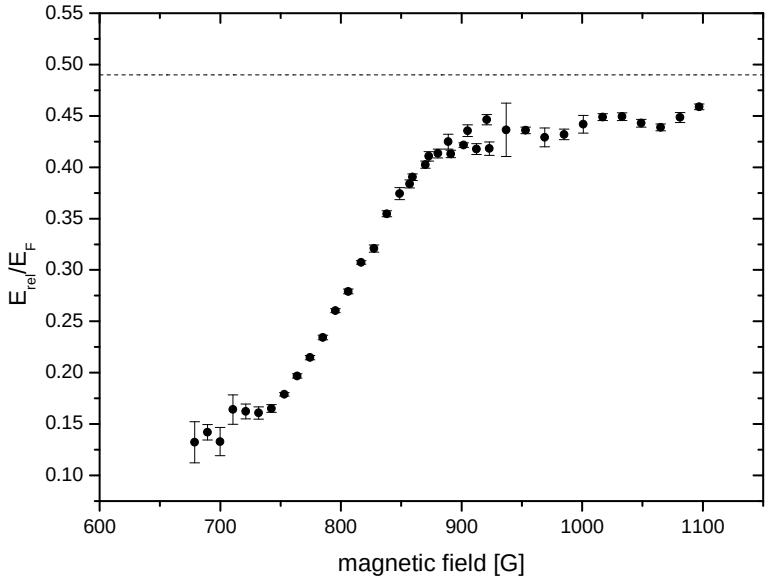

Figure 4.9: Width of an atomic cloud after $2\,\mathrm{ms}$ time of flight in dependence of the magnetic field. The errors are the statistical errors of at least five independent measurements. The dashed line indicates the theoretical width of a non-interacting ferminonic cloud.

The molecular BEC is not the actual system of interest for our experiments. It is one milestone on our way towards a mesoscopic degenerate Fermi gas. The first experiment in the cross-over from the BEC to the BCS side of the resonance is shown in figure 4.9. The plot gives the width of the atomic sample after after $2\,\mathrm{ms}$ time-of-flight for different magnetic field values. For this measurement we evaporated the sample as described above until a beam power of $300\,\mathrm{mW} \mathrel{\widehat{=}} 9\mu\mathrm{K}$ is reached. During the last $50\,\mathrm{ms}$ before the atoms are released from the trap the

magnetic field is adiabatically ramped from $751\,\mathrm{G}$ where the evaporation takes place to the probe value. The trap is compressed from $300\,\mathrm{mw}$ to $700\,\mathrm{mW}$ in $25\,\mathrm{ms}$. This ramp also starts $50\,\mathrm{ms}$ befor the trap is switched off. After $2\,\mathrm{ms}$ time-of-flight the atoms are imaged with absorbtion imaging. The resulting 2D density distribution is integrated once in the radial and once in the axial direction. A 1D Gaussian is fitted to each of the two resulting density distribution. With the obtained widths the release energy of the sample can be computed. According to [30] this can done by calculating

$$E_{rel} = \frac{1}{2} m_{\mathrm{Li}} \left(\frac{2\sigma_{rad}^2 + \sigma_{ax}^2}{\tau} \right)^2 . \tag{4.4}$$

Here σ_i is the width of the Gaussian fit for the respectiv direction an τ is the time-of-flight. Note that this equation neglegts the finite extension of the cloud in the trap. This is why the points far on the BEC side where the cloud is small, deviate a bit from the smooth decreasing of the width that is expected. The dashed line in figure 4.9 is the release energy for a ideal non-interacting Fermi gas. It was calculated by taking the momentum distribution $\hbar k$ from equation 2.47 and obtain the density distribution after $2\,\mathrm{ms}$ TOF by simply substituting $k = mx/\hbar\tau$. The resulting curve was used for a Gaussian fit and the obtained width σ_x was inserted into the equation for E_{rel}. If the gas was an ideal Fermi gas, this value should be reached on the BCS side far of resonance. However, the large negative background scattering length of $^6\mathrm{Li}$ leads to an attractive meanfield interaction. This attractive meanfield leads to a reduction of the Fermi energy and so to a lower width after expansion as for the non-interacting case.

The graph also shows that the cross-over is continuous in the interaction energy. Since the expansion at this trap depth is mainly determined by the meanfield energy of the sample, it demonstrates that the role of the repulsive interaction at positive scattering lengths is smoothly taken over by the Fermi pressure on the BCS side.

Chapter 5

Experiments in a three-component Fermi mixture

5.1 Motivation

Three component Fermi systems have been of great interest to theoretical work during the last few years. In the bosonic case, the production of trimers was predicted [31] and found [32] as the so-called Efimov states. What makes these states so special is that there is no underlying two-component bound state available in the parameter region where the trimers are formed. Either three particles are bound together or no particles are bound at all. Whether such a state also exists for a mixture of three distinguishable fermions is still a topic of discussions. There are calculations predicting such a trimer state as the energetically lowest, others suggest that dimer formation is still the dominating process in such a gas and the third particle will only remain a spectator. This could lead to a pairing competition between the different possible dimer combinations [33]. The predictions concerning the stability differ as well. It is not known, if there is a parameter regime where such a mixture is stable. At equal densities the Fermi pressure in a three component mixture is reduced, because the same momentum state can be accessed by three different fermions. The reduced Fermi pressure might lead at some point to a collapse of the gas in a so called "Ferminova" [34]. Calculations also promise a fascinating and complex phase diagram. However, up to now there has been no experimental realization of a three component Fermi mixture. This has been achieved for the first time in our experiment.

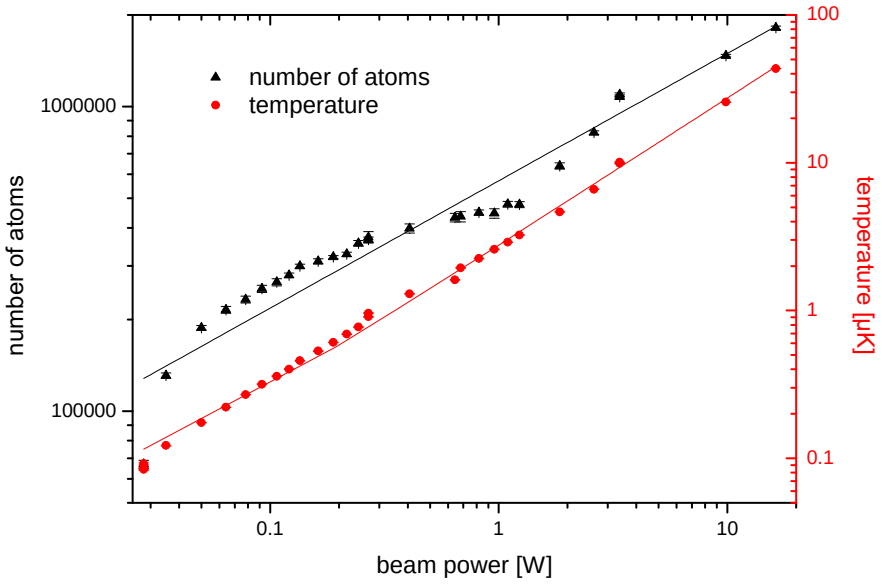

Figure 5.1: Evolution of the number of particles and their temperature during evaporation for a three component mixture. The errorbars are the statistical errors of at least five independent measurements. The fit is taken from the model given in equation 2.10 and results a truncation parameter of $\eta = 6.07(5)$. The linear fit to the temperature results $\eta = 11.2(1)$. For further evaluation of these values compare chapter 4

5.2 Sequence

To get such a mixture, the evaporation process is slightly different from the one used to produce a BEC. When the sample has reached a temperature of about $10\,\mu\mathrm{K}$ the magnetic field is ramped down to $300\,\mathrm{G}$. Here the scattering length between states $|1\rangle$ and $|2\rangle$ is small and negative, avoiding molecule formation. Molecules would complicate the production of a mixture of three spin states, since the molecules had to be broken befor flipping the spin. The released energy can result losses or heating.

The smaller scattering length has the disadvantage that more time is needed for efficient evaporation. This makes the preparation process of the spin mixture a bit more lengthy than the production of a BEC. Table 5.1 gives an overview over the laser ramps executed during forced evaporation. The efficiency of the evaporation is also reduced as can be seen in figure 5.1, where the fit reveals a truncation parameter of $\eta \approx 6$ for the AOM-controlled evaporation.

Beam power	Time	Field	Control mode
130 W→ 50 W	150 ms	751 G	Open loop
50 W→ 20 W	400 ms	751 G	Open loop
20 W→ 3.4 W	500 ms	751 G	PID loop (Si-PD)
3.4 W→ 1.4 W	500 ms	751 G	PID loop (Si-PD)
1.4 W→ 0.27 W	1500 ms	300 G	PID loop (GaAs-PD)
270 mW→135 mW	1000 ms	300 G	PID loop (GaAs-PD)
135 mW→ 28 mW	1500 ms	300 G	PID loop (GaAs-PD)
28 mW	500 ms	300 G	Plain evaporation

Table 5.1: Progress of evaporation for the preparation of a three component Fermi mixture. The table gives the ramps of the beam power, the magnetic field applied during the ramp and the mode in which the beam power is controlled.

After completing evaporation, the magnetic field is ramped up to $526\,\mathrm{G}$, where the $|1\rangle \leftrightarrow |2\rangle$ scattering length is nearly zero and the others are small and negative. Here the lifetime of the mixture is on the order of seconds, which allows to apply a RF field composed of two frequencies matching the $|1\rangle \leftrightarrow |2\rangle$ and the $|2\rangle \leftrightarrow |3\rangle$ transition for $1s$. The RF field forces the atoms to perform Rabi oscillations, which leads to a coherent superposition of the states. The Rabi frequencies were measured to be on the order of $1\,\mathrm{kHz}$. This was done by observing the time evolution of the particle number in state $|2\rangle$ during the first $2\,\mathrm{ms}$ after the RF field driving the $|2\rangle \leftrightarrow |3\rangle$ transition was switched on. The coherence is destroyed by collisions between the particles, forcing the wave function of the particles to collapse to one defined state. The collistion rate for the observed sample is about $300\,\mathrm{Hz}$. This has been calucalted by employing equation 2.46 for the peak density n. Equation 2.13 is used to calculate the scattering cross section σ with the mean scattering length $\overline{a} = -225\,a_0$. Equating the thermal energy at $10\,\mu\mathrm{K}$ with the kinetic energy $3/2\,kT = 1/2\,m_{Li}v^2 = \hbar^2k^2/2m$ the mean wavevector k and the average velocity v can be obtained. The scattering frequency can then be calculated as $\tau = n\sigma v \approx 300\,\mathrm{Hz}$. Since the pulse duration is much larger than the collision rate and the Rabi frequency, we end up with a incoherent balanced mixture off all three states.

5.3 Experimental results

Our first experiment with the prepared mixture consisted in investigating the lifetime of the mixture in dependence of the magnetic field. This was done in a first

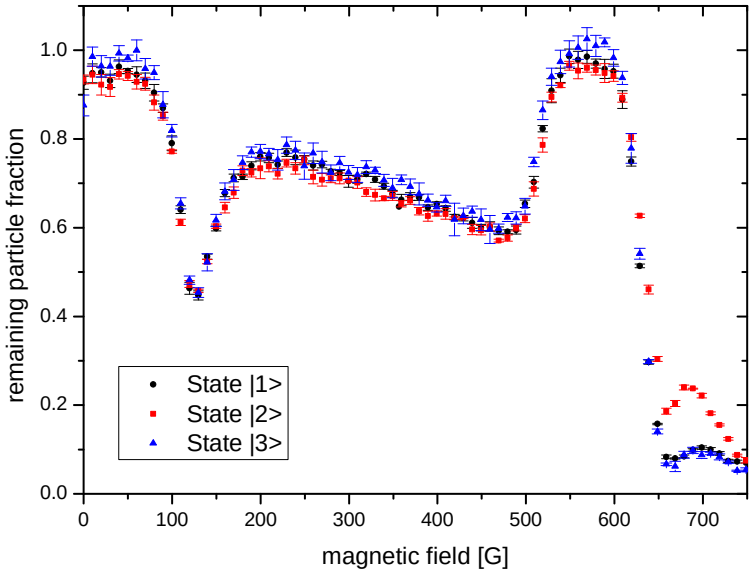

Figure 5.2: Remaining particle fraction for all three states in dependence of magnetic field. The errors are the statistical errors of at least three independent measurements.

step by ramping to the probe field after creating the mixture and measuring the remaining fraction of particles in the three states after $250\,\mathrm{ms}$ by absorption imaging. The result is given in 5.2. The graph shows a decrement of the remaining particle fraction from 0 to about $500\,\mathrm{G}$. This decrement is interrupted by a strong loss feature around $130G$ and followed by a region of stability between $540\,\mathrm{G}$ and $590\,\mathrm{G}$. At higher fields the lifetime once again decreases dramatically, revealing a difference between the three states. Particles in state $|2\rangle$ survive longer.

Searching for possible explanations for such a behavior led us to the investigation of the lifetime of a two component mixture produced under the same conditions. For this purpose we added a resonant laser pulse to the experimental sequence, removing one of the three components. The results are shown in figure 5.3. In all possible two-component mixtures there is no structure visible in these measurement, except for the expected loss feature when the magnetic field approaches the respective two particle Feshbach resonance.

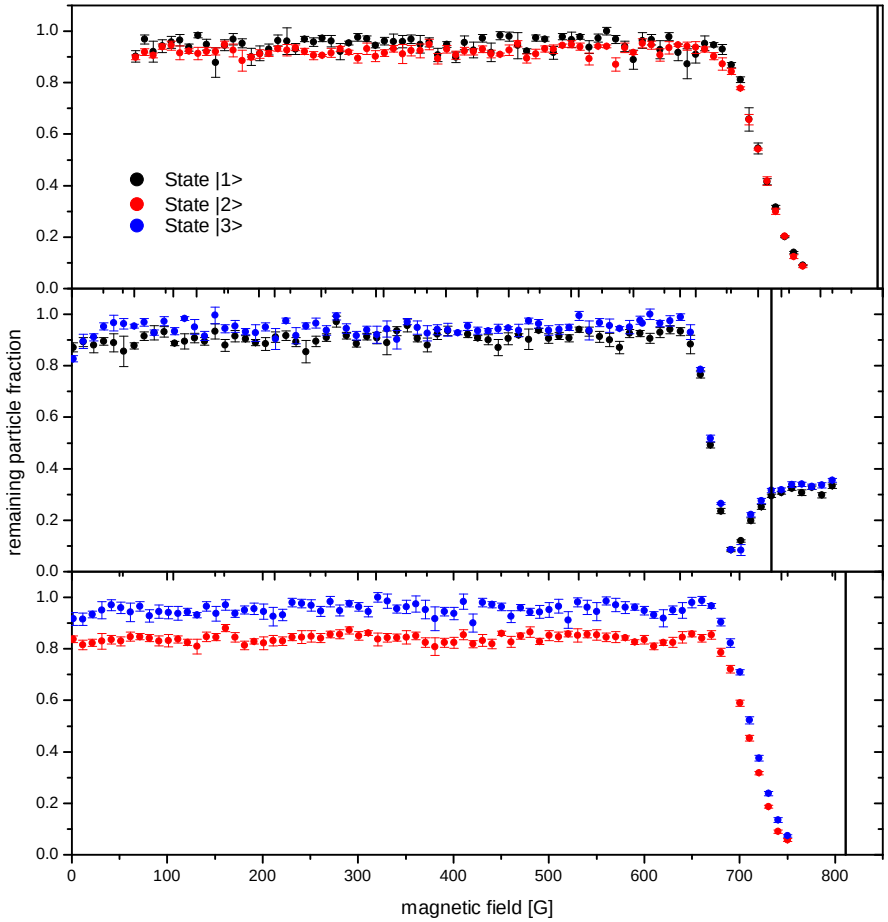

Figure 5.3: Magnetic field scan for the three possible two component mixtures. The vertical line indicates the position of the respective Feshbach resonance. The remaining particle fraction is nearly constant until the region of the Feshbach resonance is reached. The errors are the statistical errors of at least three independent measurements.

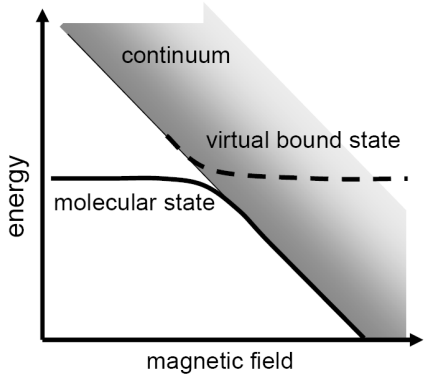

Figure 5.4: Tuning of the continuum and the molecule state with magnetic field close to a Feshbach resonance. Figure taken from [20].

5.4 Possible interpretation

Since the physics in a three component Fermi mixture is essentially not understood yet and the existing calculations do not fit our measured data, in a first step we tried to explain the behavior based on well understood two body physics. However, the fact that the reference measurement with two components reveal no structure indicates that the underlying process involves all three components.

The loss above of $600\,\mathrm{G}$ can then be explained directly by the proximity of the $|1\rangle \leftrightarrow |3\rangle$ resonance. At large positive scattering lengths molecules of particles in state $|1\rangle$ and $|3\rangle$ are formed. These molecules decay in collisions with particles from state $|2\rangle$ or with each other. The binding energy is transformed into kinetic energy and the particles can leave the trap. Since the particles of state $|2\rangle$ are not involved in the molecule formation process, the remaining fraction of these particles is significantly higher until the $|2\rangle \leftrightarrow |3\rangle$ resonance is approached. The stable region between $540\,\mathrm{G}$ and $590\,\mathrm{G}$ and below $70\,\mathrm{G}$ can also be explained by the behavior of the two body scattering lengths: In this region all three scattering lengths are small, leading to an effective reduction of the number of interacting components. A possible explanation for the decrement of the particle fraction with increasing magnetic field can be obtained from figure 5.4. This figure picture shows the tuning of the molecular state and the continuum with magnetic field. Since the molecule state is formed by two coupled channels, the molecule state and the virtual bound state undergo an avoided crossing as known for coupled two level systems in atom physics. The point of interest in this case is that the distance between the continuum and the molecular state decreases with increasing field. Therefore, it becomes more likely that the atoms enter the molecule state and get lost from the trap due to relaxation processes.

The most fascinating and least understood process is the loss feature at $130\,\mathrm{G}$.

The two body scattering lengths are small and negative at this magnetic field and show no peculiar behavior. Possible explanations are simple spin flip collision or a relaxation into deeply bound dimer states, assisted by the third component and suppressed in a two component mixture. Also likely and more interesting is the possibility of a trimer formation comparable to the Efimov state in the bosonic case. If this is the case, the three spin components could be an analogy for the three colors in QCD and further investigation could help understanding baryon formation from three quarks with different color charge.

Chapter 6

Conclusion and outlook

This thesis presented the setup of an apparatus for the creation of a highly degenerate Fermi gas. Special features of the setup are the arbitrary tunability of the interactions between particles by means of Feshbach resonances as well as the possibility to shape the trapping potential nearly at will with two perpendicular AOMs. The dipole trap was caracterized by means of the trap frequencies and the heating rate. The apparatus can create a molecular BEC within less than $4\,\mathrm{s}$, making it one of the fastest in the world. It is also very reliable, since it works nearly without maintenance. Usually neither of the partly very sensitive allignments of the lasers have to be realigned within weeks. Even after a complete dismantling of the MOT and major changes in the setup, the apparatus was ready to preform measurements within an hour. This can partly be attributed to the fact that the group persuits of keeping things simple and falling back on established techniques wherever they are available. All this makes working with the apparatus very efficient and convenient.

In the following chapters first experiments in the dipole trap were presented. The evaporation and the formation of molecules were characterized. The condensate defied quantitative analyses and comparison with theory due to the large mean-field interaction. This will certainly become possible as soon as the cloud can be imaged in-situ with the high resolution imaging.

The fifth chapter explained the creation of a three component Fermi mixture and first lifetime measurements in such a sample. The results are published in our first paper [35]. The most exciting detail of the graph plotting the remaining fraction of atoms in the trap after $250\,\mathrm{ms}$, is a loss feature at $130\mathrm{G}$. The physics we are observing here has definitely attract attention, especially theoretician's. The discussion about the origin of this loss feature is still in progress. Priliminary calculations of D. Petrov very recently showed that our measurements can qualitatively be reproduced by assuming two trimer states crossing the continuum. Choosing the real and the imaginary part of the three body parameter adequately, his results

agree with the shape of our measured curve. It is the first theoretical indication that the three body loss process might actually be traced back to trimer formation.

In the future we want to concentrate on two subjects: The creation and investigation of few fermion quantum systems and further experiments with the three-component mixture. With the few Fermion system we hope to gain better understanding of many-body physics. Our experiment opens up the possibility to investigate these systems in a variety of regimes that could not be accessed in previous experiments. This might enlarge our knowledge about few particle physics. When the imaging system is optimized to resolve single particles, we might be able to observe the formation of pairs in momentum space or the emergence of shells. Exciting and observing collective oscillations will possibly result in a better understanding of giant resonances observed in atomic cores.

In the three-component mixture we will first try to understand the process of pairing. Proving experimentally that trimers are formed is the next step in this process. Thereafter we will try to observe meanfield effects in this system. Here the points of interest are collective oscillations or indications for superfluiditiy.

To answer these questions experimentally we will first have to finish the setup of the high resolution imaging (HRI). The asphere has already been implemented into the setup and first images in the vertical axis have been taken. A test of the setup revealed a resolution of $2\,\mu\mathrm{m}$, nearly one order of magnitude better than the currently used imaging system. This will allow for imaging the particles directly in the trap. Only minor problems have to be solved to start working with this new imaging system.

We will then continue our investigation of the three component mixture. We will try to examine the pairing behavior of the three components by doing RF spectroscopy. Also, if there is phase separation of different states or of bound and unbound atoms, this will be seen with the HRI. After that, we will try to excite collective oscillations to learn more about the manybody properties of the sample. And perhaps it will even be possible to observe vortices in the trap and so prove the existence of superfluidity in the sample.

The last step towards the creation and observation of a few fermion degenerate quantum gas is the setup of the micro trap. For this purpose, two AOMs (for scanning and controlling the intensity of the beam) and a dicroic cube (for combining trap and imaging beam) have to be bought and brought into position. Getting all the elements to work together will certainly be a challange. Yet if things go as well as they went for the last year, I am positive that we will be able to explore a wide field of new and intriguing physis very soon.

Appendix

Fundamental constants

Symbol	Value	Meaning
$\hbar$	$1.054571628\times10^{-34}\,\mathrm{Js}$	Planck's constant over 2π
c	$2.99792458\times10^{8}\,\mathrm{m/s}$	Speed of light in vacuum
k_B	$1.3806504\times10^{-23}\,\mathrm{JK}^{-1}$	Boltzmann's constant
a_0	$0.52917720859\times10^{-10}\,\mathrm{m}$	Bohr's radius
ϵ_0	$8.854187817\times10^{-12}\,\mathrm{Fm}^{-1}$	Electric constant
m_{Li}	$9.98834146\times10^{-27}\,\mathrm{kg}$	Mass of a ^{6}Li atom
Γ_{Li}	$36.898\times10^{6}\,\mathrm{s}^{-1}$	Natural linewidth of the D_2 line of ^{6}Li
λ_{Li}	$670.977338\times10^{-9}\,\mathrm{m}$	Wavelength of the D_2 line of ^{6}Li in vacuum

Table 6.1: Constants used in this thesis. The fundamental constants are taken from [36], the properties of ^{6}Li can be found in [37].

Bibliography

[1] S. Chu, J. E. Bjorkholm, A. Ashkin, and A. Cable. Experimental observation of optically trapped atoms. *Phys. Rev. Lett.*, 57(3):314–317, Jul 1986.

[2] M. H. Anderson, J. R. Ensher, M. R. Matthews, C. E. Wieman, and E. A. Cornell. Observation of Bose-Einstein condensation in a dilute atomic vapor. *Science*, 269:198–201, Jul 1995.

[3] K. B. Davis, M. O. Mewes, M. R. Andrews, N. J. van Druten, D. S. Durfee, D. M. Kurn, and W. Ketterle. Bose-Einstein condensation in a gas of sodium atoms. *Phys. Rev. Lett.*, 75(22):3969–3973, Nov 1995.

[4] J. Stenger, S. Inouye, M. R. Andrews, H.-J. Miesner, D. M. Stamper-Kurn, and W. Ketterle. Strongly enhanced inelastic collisions in a Bose-Einstein condensate near Feshbach resonances. *Phys. Rev. Lett.*, 82(12):2422–2425, Mar 1999.

[5] C. A. Regal, C. Ticknor, J. L. Bohn, and D. S. Jin. Creation of ultracold molecules from a Fermi gas of atoms. *Nature*, 424(6944):47–50, 2003.

[6] M. Greiner, C. A. Regal, and D. S. Jin. Emergence of a molecular Bose-Einstein condensate from a Fermi gas. *Nature*, 426:537–540, 2003.

[7] S. Jochim, M. Bartenstein, A. Altmeyer, G. Hendl, S. Riedl, C. Chin, J. Hecker Denschlag, and R. Grimm. Bose-Einstein condensation of molecules. *Science*, 302(5653):2101–2103, 2003.

[8] M. W. Zwierlein, C. A. Stan, C. H. Schunck, S. M. F. Raupach, S. Gupta, Z. Hadzibabic, and W. Ketterle. Observation of Bose-Einstein condensation of molecules. *Phys. Rev. Lett.*, 91(25):250401, Dec 2003.

[9] J. Bardeen, L. N. Cooper, and J. R. Schrieffer. Theory of superconductivity. *Phys. Rev.*, 108(5):1175–1204, Dec 1957.

[10] C. A. Regal, M. Greiner, and D. S. Jin. Observation of resonance condensation of fermionic atom pairs. *Phys. Rev. Lett.*, 92(4):040403, Jan 2004.

[11] M. Bartenstein, A. Altmeyer, S. Riedl, S. Jochim, C. Chin, J. Hecker Denschlag, and R. Grimm. Crossover from a molecular Bose-Einstein condensate to a degenerate Fermi gas. *Phys. Rev. Lett.*, 92(12):120401, Mar 2004.

[12] Ákos Rapp, Gergely Zaránd, Carsten Honerkamp, and Walter Hofstetter. Color superfluidity and "baryon" formation in ultracold fermions. *Phys. Rev. Lett.*, 98:160405, 2007.

[13] Friedhelm Serwane. The setup of a magneto optical trap for the preparation of a mesoscopic degenerate Fermi gas. Diploma thesis, 2007.

[14] Thomas Lompe. An appartus for the production of molecular Bose-Einstein condensates. Diploma thesis, 2008.

[15] Harold J. Metcalf and Peter van der Straten. *Laser Cooling and Trapping*. Springer-Verlag, New York, 1999.

[16] M. Weidemüller R. Grimm and Y. B. Ovchinnikov. Optical dipole traps for neutral atoms. *Advances in Atomic, Molecular and Optical Physics*, 42:95, 2000.

[17] Bahaa E. A. Saleh and Malvin Carl Teich. *Fundamentals of Photonics*. John Wiley and Sons, Inc., 1991.

[18] K. M. O'Hara, M. E. Gehm, S. R. Granade, and J. E. Thomas. Scaling laws for evaporative cooling in time-dependent optical traps. *Phys. Rev. A*, 64(5):051403, Oct 2001.

[19] Paul Julienne. Private communications, calculations done according to [22].

[20] Selim Jochim. *Bose-Einstein Condensation of Molecules*. PhD thesis, Universität Innsbruck, 2004.

[21] Herman Feshbach. A unified theory of nuclear reactions. *Ann. Phys.*, 5(337), 1958.

[22] M. Bartenstein, A. Altmeyer, S. Riedl, R. Geursen, S. Jochim, C. Chin, J. Hecker Denschlag, R. Grimm, A. Simoni, E. Tiesinga, C. J. Williams, and P. S. Julienne. Precise determination of ^{6}Li cold collision parameters by radio-frequency spectroscopy on weakly bound molecules. *Physical Review Letters*, 94(10):103201, 2005.

[23] Lev Pitaevskii and Sandro Stringari. *Bose-Einstein Condensation*. Oxford Science Publications, 2003.

[24] L. P. Pitaevskii F. Dalfovo, S. Giorgini and S. Stringari. Theory of Bose-Einstein condensation in trapped gases. *Rev. Mod. Phys.*, 71(3):463–512, Apr 1999.

[25] S. Giorgini, L. P. Pitaevskii, and S. Stringari. Condensate fraction and critical temperature of a trapped interacting Bose gas. *Phys. Rev. A*, 54(6):R4633–R4636, Dec 1996.

[26] D. A. Butts and D. S. Rokhsar. Trapped Fermi gases. *Phys. Rev. A*, 55(6):4346–4350, Jun 1997.

[27] Wolfgang Nolting. *Grundkurs Theoretische Physik 6: Statistische Physik*. Springer Verlag Berlin Heidelberg, 5 edition, 2005.

[28] M. W. Zwierlein, J. R. Abo-Shaeer, A. Schirotze, C. H. Schunck, and W. Ketterle. Vortices and superfluidity in a strongly interacting Fermi gas. *Nature*, 435:1047–1051, 2005.

[29] J. Dalibard and C. Cohen-Tannoudji. Dressed-atom approach to atomic motion in laser light: the dipole force revisited. *Journal of the Optical Society of America B*, 2(11):1707, 1985.

[30] T. Bourdel, L. Khaykovich, J. Cubizolles, J. Zhang, F. Chevy, M. Teichmann, L. Tarruell, S. J. J. M. F. Kokkelmans, and C. Salomon. Experimental study of the BEC-BCS crossover region in Lithium 6. *Physical Review Letters*, 93(5):050401, 2004.

[31] V. Efimov. Weakly-bound states of three resonantly-interacting particles. *Sov. J. Nucl. Phys.*, 12:589–595, 1971.

[32] H.-C. Nägerl, T. Kraemer, M. Mark, P. Waldburger, J. G. Danzl, B. Engeser, A. D. Lange, K. Pilch, A. Jaakkola, C. Chin, and R. Grimm. Experimental evidence for Efimov quantum states in an ultracold gas of caesium atoms. *Nature*, 440:315, Mar 2006.

[33] T. Paananen, J.-P. Martikainen, and P. Törmä. Pairing in a three-component Fermi gas. *Phys. Rev. A*, 73(5):053606, 2006.

[34] D. Blume, Seth T. Rittenhouse, J. von Stecher, and Chris H. Greene. Stability of inhomogeneous multicomponent Fermi gases. *Phys. Rev. A*, 77(3):033627, 2008.

[35] T. B. Ottenstein, T. Lompe, M. Kohnen, A. N. Wenz, and S. Jochim. Collisional stability of a three-component degenerate Fermi gas. *arxiv.org*, 0806:0587, 2008.

[36] NIST. http://physics.nist.gov/cuu/constants/.

[37] M. E. Gehm. Properties of $^6\mathrm{Lithium}$, 2003: *http://www.phy.duke.edu/research/photon/qoptics/techdocs/pdf/PropertiesOfLi.pdf*.

Danksagung

Ich möchte ein paar Menschen danken, die in ihrer jeweiligen Art und Weise mich bei der Erstellung dieser Arbeit unterstützt haben und ohne die diese Arbeit so nicht hätte zu Stande kommen können:

Zunächst möchte ich Selim danken, dass er mir die Möglichkeit gegeben hat, in seiner Gruppe zu arbeiten. Für seine Bereitschaft, immer da zu sein, wenn es Fragen und Probleme gab, für seine Geduld, wenn er mir etwas erklärte und für seine Unterstützung in so vielen Belangen.

Dafür danke ich auch der ganzen Gruppe: Timo, Thomas, André, Gerhard und Friedhelm, mit denen ich ein spannendes und lehrreiches Jahr verbringen durfte, von denen ich viel gelernt und auch viel Hilfe erfahren habe.

Ich danke Alexander Dorn, dass er die Zweitkorrektur dieser Arbeit übernimmt und David Zorn für die Hilfe bei der sprachlichen Optimierung.

Ich danke Moritz und Tobias, die mich das ganze Studium über begleitet haben und ohne die ich vielleicht schon nach den ersten Übungszetteln aufgegeben hätte.

Ich danke meinen jetztigen und ehemaligen Mitbewohnern im AMH, besonders M.K., moje słoneczko, für so viele schöne Stunden. Ich durfte eine Gemeinschaft erleben, die mich nach so manchem schweren Tag aufgefangen und aufgebaut hat. Es hat einen unschätzbaren Wert, vier schöne Jahre mit euch verbringen zu dürfen, und ich danke euch dafür von ganzem Herzen.

Danken möchte ich auch meiner Familie, meinen Eltern und Geschwistern, für eine Unterstützung, die die Dauer dieses Studiums um ein Weites übertrifft. Das Glück, eine Familie zu haben, auf die man sich verlassen kann und die immer bereit ist, einem den Rücken zu stärken, ist nicht selbstverständlich und Anlass zu großer Dankbarkeit.

Das, was wir sind und was wir vollbringen, ist letztlich nicht unser eigener Verdienst und unsere eigene Leistung. Es ist ein Geschenk. Ich bin dankbar und glücklich, das ich so reich mit Gutem beschenkt wurde und werde.

Erklärung:

Ich versichere, dass ich diese Arbeit selbstständig verfasst und keine anderen als die angegebenen Quellen und Hilfsmittel benutzt habe.

Heidelberg, den _____ _____

Unterschrift